frontiers in Earth Science

ORIGINAL RESEARCH
published: 09 March 2022
doi: 10.3389/feart.2022.852786

Hydrothermal Vent Complexes Control Seepage and Hydrocarbon Release on the Overriding Plate of the Tyrrhenian-Ionian Subduction System (Paola Basin)

Marzia Rovere[1]*, *Alessandra Mercorella*[1], *Fabiano Gamberi*[1] and *Fabrizio Zgur*[2]

[1]Istituto di Scienze Marine, Consiglio Nazionale Delle Ricerche, Bologna, Italy, [2]Osservatorio Geofisico Sperimentale, Sgonico, Trieste, Italy

Active fluid seeps have been described in a wide range of geological environments and geodynamic contexts, which include continental shelves of non-volcanic passive margins and accretionary wedges. Fluids seeping in hybrid volcanic-sedimentary basins, characterized by the presence of magmatic intrusive complexes, have always received less attention. We detected and imaged dozens of distinct gas flares, as high as 700 m, on the continental slope of the Paola Basin in the southeastern Tyrrhenian Sea, at 550–850 m water depth. The sedimentary basin is surrounded by Pleistocene active and inactive volcanoes and volcanic-intrusive complexes, which formed in the back-arc basin of the Calabrian subduction zone, in response to subduction-induced mantle flow. Gas flares develop above pockmarks, craters and mud flows that form over and along the scarps of mound structures and correspond to seismic zones of free gas accumulation in the sub-seafloor. Here, methane-derived siderite shows enrichment in $\delta^{13}C$ and $\delta^{18}O$ isotopes likely related to methanogenesis and intermittent venting of deep-sourced CO_2. Multichannel seismic reflection data showed that the gas flares develop in correspondence of doming and diapirism apparently originating from the top of the Messinian evaporites and nearby magmatic sills, that are present in the lower part of the Plio-Quaternary succession. These diapiric structures can be related to seafloor hydrothermal vent complexes fed by the igneous intrusions. Our data suggest that the vent complexes acted as fluid migration pathways and gas conduits, which at times are bounded by deep-rooted normal faults, leading to post-explosive near-surface microbial activity and seep carbonate formation. Fluids being mobilised by magmatism in the study area include: hydrocarbons and hydrothermal fluids generated at depth, interstitial water expelled during formation of polygonal faults. The close spatial correlation between seafloor seep manifestations, fluid migration pathways in the sub-surface involving part of the Messinian units and igneous features indicates that magmatic activity has been the main driver of fluid flow and can have a long-term effect in the southern Tyrrhenian Sea.

Keywords: gas flares, hydrothermal vent complex, Messinian evaporites, Mediterranean Sea, methane-derived carbonates

OPEN ACCESS

Edited by:
Miriam Römer,
University of Bremen, Germany

Reviewed by:
Srikumar Roy,
University College Dublin, Ireland
Claudio Argentino,
UiT The Arctic University of Norway, Norway

***Correspondence:**
Marzia Rovere
marzia.rovere@cnr.it

Specialty section:
This article was submitted to Marine Geoscience, a section of the journal Frontiers in Earth Science

Received: *11 January 2022*
Accepted: *08 February 2022*
Published: *09 March 2022*

Citation:
Rovere M, Mercorella A, Gamberi F and Zgur F (2022) Hydrothermal Vent Complexes Control Seepage and Hydrocarbon Release on the Overriding Plate of the Tyrrhenian-Ionian Subduction System (Paola Basin). Front. Earth Sci. 10:852786. doi: 10.3389/feart.2022.852786

INTRODUCTION

The release of carbon-bearing gases from the seafloor into the water column is generally classified into: high-temperature hydrothermal vent complexes (HTVC), releasing gas rich in inorganic carbon dioxide (CO_2), typically produced by thermo-metamorphism of limestones or magma-mantle degassing (e.g. the Guaymas Basin, Berndt et al., 2016); low-temperature cold seep systems, releasing mainly biotic methane (CH_4) and other hydrocarbons, produced by microbial or thermogenic degradation of organic matter in sedimentary basins (e.g., the Cascadia margin, Riedel et al., 2018).

In many cases, however, magmatic intrusions and volcanic plumbing systems occur within sedimentary basins resulting in hybrid systems with both CO_2-rich geothermal fluids and CH_4-rich biotic gas (microbial or thermogenic) sourced from the organic-rich sediments (Procesi et al., 2019).

The importance of hybrid geological systems, hosting both volcano-hydrothermal and sedimentary components, was first recognized by Svensen et al. (2003), who noted that deep sedimentary basins affected by circulation of magmatic fluids or by the intrusion of igneous rocks, may result in the migration of a combination of fluids, hot water and gases, accompanied by precipitation of authigenic carbonates.

Evidence is growing that intrusive magmatic bodies, such as sills, can influence the long-term migration of fluids from the deep subsurface to form HTVCs that can be reutilized as focused areas of fluid flow (Lawrence and Cartwright, 2010; Rollet et al., 2012; Roelofse et al., 2021). This influence is largely due to permeability contrasts between the intrusion and the host sediment or to interconnected open fractures and faults within and around intrusions acting as conduits for migrating fluids (Omosanya et al., 2018). Large-scale fractures and fault can provide discontinuities with increased sediment permeability, that can represent further conduits for fluid and gas transport in seep sedimentary environments (e.g., Plaza-Faverola et al., 2015), allowing hydrocarbon-rich fluids from greater depth to reach shallow sediments and the sediment-water interface. Furthermore, also salt diapirs have been connected to seepage of gas to the seabed in different geological contexts (Serié et al., 2012; de Mahiques et al., 2017; Madof, 2018; Müller et al., 2018).

Sedimentary basins in geodinamically active regions, such as back-arc basins, host deep and permeable fault and fracture systems that can act as pathways for the migration of deep crustal or mantle gases (CO_2-rich) favouring their mixing with shallower sedimentary (CH_4-rich) gases. In these basins, the tectonic extensional regime can also allow for the emplacement of sills and/or magma intrusions, not necessarily leading to active volcanic centers. Sills typically penetrate only the bottom of the sedimentary formations (De Ritis et al., 2019).

Past hybrid systems are common, both on land and in the offshore: in the large igneous provinces of the Karoo Basin in South Africa (Svensen et al., 2006), offshore northeast Greenland (Reynolds et al., 2017), in the Vøring and Møre Basins of the North Sea (Omosanya et al., 2018), offshore NW Australia (Magee et al., 2016). However, modern hybrid systems remain overlooked, although are important because: i. they may lead to production of hydrocarbons from enhanced thermal maturity of sedimentary rocks (Sydnes et al., 2019); ii. depending on the water depth, can be natural sources of greenhouse gas to the atmosphere (McGinnis et al., 2006); iii. are potential drivers of past climate change (Svensen et al., 2004; Iyer et al., 2013).

An extensive hydroacoustic mapping campaign including water column recording, sub-bottom sediment profiling and multichannel seismic acquisition has been conducted in the Paola Basin, in the back-arc domain of the southern Tyrrhenian Sea. This contribution aims at showing how flares, indicative of gas bubble release, are widespread in the water column, and what is their relationships with seismic features indicative of subsurface gas, and morphologic elements suggestive of seafloor venting. We also discuss the origin of the fluids in the frame of the tectonic and volcanic regime of the Tyrrhenian back-arc area in the context of its subduction-related geodynamic setting.

Study Area

The Paola Basin lies at the rear of the Calabrian Arc, in the upper plate of the northwestward dipping Tyrrhenian-Ionian subduction system, which includes the back-arc domain of the SE Tyrrhenian Sea, volcanic seamounts, the Aeolian Islands volcanic arc and the fore-arc region of the Calabrian accretionary wedge (**Figure 1A**). The basin formed since the late Miocene, as a result of compressional (Pepe et al., 2010) and strike-slip (Milia et al., 2009) tectonics, in an overall extensional regime.

The Paola Basin area is flanked to the north and west by active and inactive volcanoes. In the north, the area is characterized by the presence of magmatic intrusions that locally reach the seafloor forming the Diamante and Enotrio volcanic edifices and the flat-topped Ovidio Seamount (Würtz and Rovere, 2015, **Figure 1B**). Altogether, these form a volcanic-intrusive complex characterized by a deep-rooted, magma feeding system, formed in consequence of the ascent of subduction-induced mantle flow originated in the northwestern edge of the retreating ionian slab (De Ritis et al., 2019). The volcanoes are not presently active even if hydrothermal activity occurs, as the emplacement and cooling of the magma occurred sometime during the Brunhes Chron (De Ritis et al., 2019).

The Alcione Seamount is a ~1,000 m-high conical volcano located on an almost flat seafloor on the lower slope of the Paola Basin (Marani and Gamberi, 2004) and is characterized by absence or very weak hydrothermal activity (Lupton et al., 2011). The Lametini Seamounts are two conical edifices on top of which Fe-Mn crusts characterized by a very low Fe/Mn ratio and high Cu-content indicative of hydrothermal venting were dredged (Rossi et al., 1980) (**Figure 1B**).

A 60-km-long anticline (Paola Ridge, **Figure 1A**) bounds westward the Paola Basin syncline (Gamberi and Rovere, 2010). Here, cold seep-like structures were discovered with

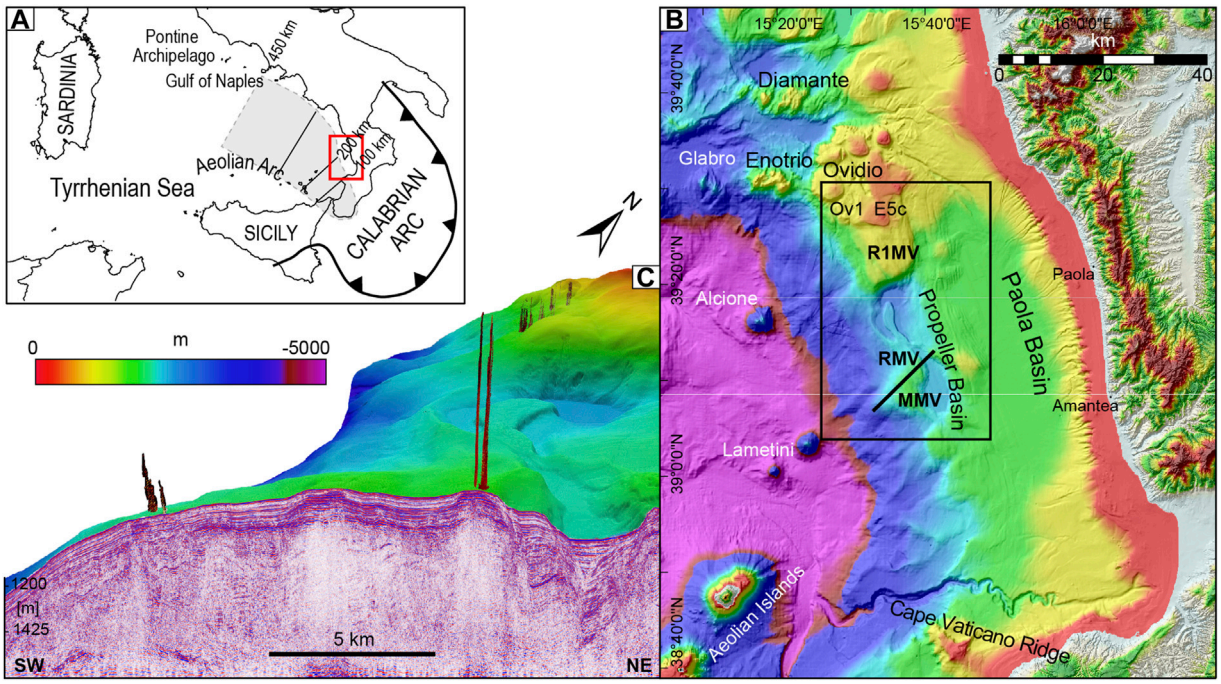

FIGURE 1 | (A) Sketch of the geodynamic setting of the southern Tyrrhenian Sea and Calabrian Arc with the outlines of the depths (from Chiarabba et al., 2008) of the northwestward dipping slab of the Tyrrhenian-Ionian subduction system. The red rectangle is the focus area imaged in **(B)**. **(B)** Bathymetry of the Paola Basin and the surrounding areas, the black rectangle outlines the study area of **Figure 2**. **(C)** 3D scene of the gas flares in the water column superimposed to a multichannel seismic reflection (MCS) profile whose track line is located in **(B)**.

full-ocean depth multibeam and backscatter data at 500–800 m water depth. Higher resolution acquisitions and seafloor sampling were carried out in 2011 (Rovere et al., 2014). The most prominent structures in the area are represented by three mound structures (RMV, MMV and R1MV, **Figure 1B**) which make up the Paola Ridge and stand 200–400 m above the Propeller Basin located landward (**Figure 1B**). Active gas venting at the seafloor was detected via multibeam echosounder at RMV location (Rovere et al., 2014), while oxy-hydroxides (goethite), sulfides (pyrite, marcasite and sphalerite) and siderites were collected in the sub-seafloor of all mounds (Rovere et al., 2015). Siderites precipitated in burrows and hardgrounds in the shallower sedimentary succession showing enrichment in $\delta^{13}C$ (3–10 V-PDB ‰) and $\delta^{18}O$ (8–9 V-PDB ‰) isotopes, which are compatible with their precipitation in the methanogenic zone (Rovere et al., 2015) during periods of lower gas discharges under prolonged anoxic conditions and intermittent venting of deep-sourced CO_2 (Franchi et al., 2017).

NW-SE and NNW-SSE-oriented normal faults, which can be regarded as the marine prolongation of the fault zones that dissect the Calabrian Arc from SE to NW, were suggested to be the most probable mechanism for the emplacement of the mud mobile structures and primary conduits for upward fluid migration (Rovere et al., 2014). It was further noted that the mound structures rise in coincidence with extensional faults that offset the Messinian evaporites, suggesting that pre-Messinian source rocks, mobilized along discrete belts of active tectonic deformation, were controlling the seepage of fluids in the study area (Gamberi and Rovere, 2010).

MATERIALS AND METHODS

The data for this study were acquired during the R/V Urania cruise MarBeep in 2014. The track lines in **Figure 2A** show the multichannel seismic reflection survey (MCS) and the location of the CROP M36 and other vintage seismic reflection data used for the seismostratigraphic correlations in the study area.

Hydroacoustic Data

The acoustic detection of the water column flares was performed using Kongsberg EM710 (100 kHz, 1° × 1°) and EM302 (30 kHz, 1° × 2°) multibeam systems (MBES) that were both hull-mounted on board the R/V Urania. Bathymetric data were also collected and integrated the seafloor coverage achieved during the previous campaign carried out in 2011 (Rovere et al., 2014). Sound velocity profiles were obtained with a Seabird-Scientific SBE 911 plus CTD unit mounted on a rosette carrying 24 Niskin bottles and were applied both in real-time acquisition and post-processing. Bathymetric and seafloor reflectivity data were post-processed using the suite CARIS HIPS & SIPS.

Water column data were extracted mainly from EM302 data after quality check and processed with the QPS Fledermaus (version 7.8, including the FMMidwater module) software package which allows for manual flare identification and geo-

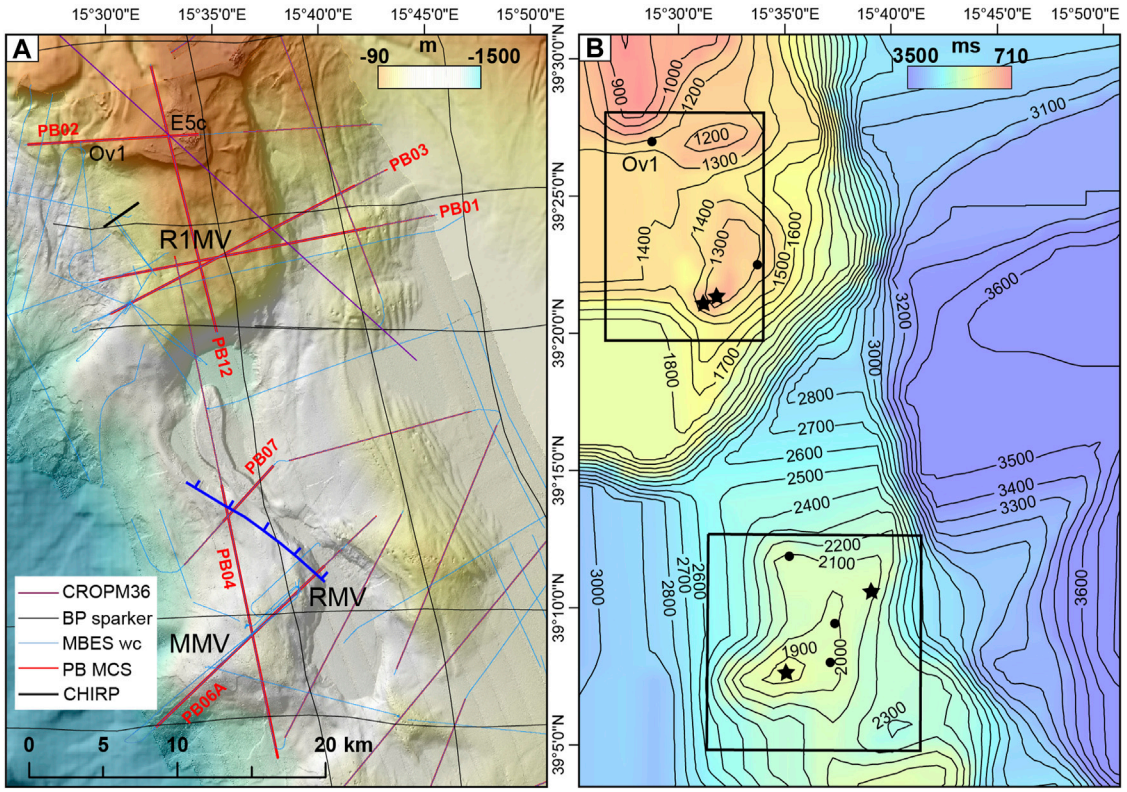

FIGURE 2 | (A) High resolution bathymetry of the Paola Ridge with track lines of the MCS and sparker data used to reconstruct the depth of the top of the Messinian units (MES) in **(B)**. The traces of water column acoustic recording by multibeam echosounders are presented and the portion of MCS profiles displayed in **Figures 3**–**8**, **11** are marked in bold. **(B)** The depth of the Messinian reflector (MES) is displayed in ms TWT with superimposed contour lines every 100 ms. Stars and circles indicate culmination of diapirs originated from updoming of the Messinian units with and without gas flares, respectively. The two rectangles outline the northern and southern sectors shown in **Figures 9**, **10**.

picking of flare sources. A normalization filter was applied to identify background noise values (dB) and apply signal-to-noise level thresholds (see Rovere et al., 2020 for a complete description of the processing routine). Water column plume features (flares) were manually extracted and exported as ASCII points, including longitude, latitude, depth of the feature and signal amplitude (dB) corrected with sound velocity profiles. The georeferenced seep data were imported into the Fledermaus software to explore virtual 3D scenes containing digital elevation models of the seafloor and sub-seafloor (**Figure 1C**). Geographical visualization and statistical analysis were performed using ESRI ArcMap 10.8. The relative height of the flares was obtained using the spatial analyst tool "extract multi value points" applied to the raster obtained from the bathymetric data acquired simultaneously with the water column.

Bottom waters were collected with a box-corer from the two most energetic gas discharging locations (R1MV and RMV), one of which already identified and imaged (Rovere et al., 2014). Water samples were taken immediately and bubble free after retrieval using a silicon tube. Samples were directly transferred into 250 ml pre-evacuated glass flasks and were acidified with 2 ml 37% HCl. The bottles were sealed with a Teflon-coated butyl rubber seal and were closed with aluminum crimp caps. Five additional near-bottom water samples were collected by means of the rosette sampler alongside the two most energetic structures. Dissolved gas concentrations were determined applying headspace analysis and gas chromatography techniques described in Franchi et al. (2017).

Seismic Reflection Data

Multichannel seismic reflection profiles (MCS, **Figure 2A**) were acquired by a single 60 in^3 mini Sercel GI-gun set in Harmonic Mode (30 Generator +30 Injector) with a shot interval of 9.375 m at 2000 psi. The data were collected by a 300 m long, 96 channels Geometrics GeoEel digital streamer with a trace distance of 3.125 m. Both the gun and the streamer were towed at 1.5 m below sea level to minimize the ghost effect on the emitted spectrum (centered well above 200 Hz), thus preserving the high frequencies needed to better resolve the shallower targets. During the acquisition four Digicourse birds were used to keep the streamer at a constant depth. The acquisition setting allowed a compromise between penetration in 700–800 m water depth and resolution, which can be regarded as metric along the vertical axes, if assuming a λ/4 criterion, with an actual 1.56 m lateral distance between the traces in the stack section. With this configuration, resulting in an effective horizontal sampling of

1.56 m in the stacked section, the maximum attainable fold coverage was 16 traces/CDP. The polarity of the seismic data was recorded as minimum-phase reverse SEG Standard. A conventional processing was applied by means of the Schlumberger Vista package; the sequence consisted of shot gather editing, large band pass filtering, velocity analyses, velocity based spherical divergence compensation, NMO correction, stack in common midpoint domain. The stack sections were eventually time migrated.

MCS profiles were further treated for image visualization with the Geosuite AllWorks software in which an A.G.C. window length of 250 ms was added to enhance the deeper reflections. The Petrel E&P Software Platform was used to extract the Root Mean Square (RMS) amplitude (iterative) attribute and to detect bright spots.

Vintage sparker profiles were made available by the Institute of Marine Sciences as paper profiles that were scanned to high resolution raster image (TIFF) and converted into georeferenced SEGY format using the Matlab routine IMAGE2SEGY (Farran, 2008).

The reflector corresponding to the top of the Messinian units (MES) was mapped on available MCS and sparker profiles and interpolated with spherical kriging with 1 km radius; contours were extracted as isobaths expressed in ms TWT (**Figure 2B**).

The seismic data are presented in TWT, as an accurate depth conversion is not feasible due to the lack of boreholes and a proper velocity model. However, some features are described in distance-depth and the thickness of sediment and volcanic deposits were derived from time to depth conversion using velocities of 1,500 and 2,100 m/s for respectively the water column and the Plio-Quaternary deposits, for consistency with De Ritis et al. (2019).

Sub-bottom echosounder profiles were used to image shallow sedimentary structures and map gas indicators with a Teledyne Benthos CHIRP-III system. The system is comprised of a 16 hull-mounted transducer array with a 2–20 kHz sweep-modulated bandwidth and 4 kW power per-channel, which allows a vertical resolution of about 50 cm. Data were post-processed for trace equalization and band-pass filtering with the software Geosuite All Works. Calculations for converting from two-way-traveltime to depth used a sound velocity of 1,500 m/s.

Indicators of Gas and Magmatic Features in Marine Geophysical Data

In seismic reflection data, bright spots and high-amplitude anomalies, seismic attenuation, velocity pull-down events, flat spots and chimneys are indicative of the presence of gas in the sediment and fluid contact (Müller et al., 2018). In our seismic data, gas-induced bright spots have the characteristic "peak-over-trough" pattern, in which a high-amplitude trough follows a high amplitude peak (a decrease in acoustic impedance, negative amplitude anomaly). On the contrary, the trough-over-peak reflections or positive amplitude anomalies represent a transition to a harder material (increase in acoustic impedance) generally associated with the occurrence of denser sediments, hardgrounds, precipitated authigenic carbonates, gas hydrates or the seabed.

Furthermore, in seep environments pull-up events may be caused by the presence of rocks with higher seismic velocity than the strata above, such as authigenic carbonates (Madof, 2018).

Magmatic sills can be interpreted based on their high amplitude character, showing as localized brightening of positive amplitude reflections similar to the seabed reflector (Omosanya et al., 2018). In terms of geometry and lateral continuity within the host strata, sills are imaged in seismic reflection data as saucer-shaped or sheet-like, high-amplitude reflections with abrupt lateral terminations within the host-rock strata (Roelofse et al., 2021).

Hydrothermal vent complexes are imaged on seismic sections as pipe-like, vertical zones of low amplitude and chaotic reflections in the conduits, terminating as dome, eye-shaped or crater morphologies at their summits (Omosanya et al., 2018). The interior of the vents vary between chaotic seismic reflections and clear reflections that terminate within the vents as a result of the disruption of the originally stratified sedimentary rock during fluid expulsion (Roelofse et al., 2021).

In side-scan sonar and multibeam backscatter data, the recognition of seep sites on the seafloor is often favoured by the detection of anomalously high acoustic seafloor reflectivity, caused by enhanced acoustic impedance contrast related to: sharp changes in the seafloor morphology (pockmarks, mud volcanoes); precipitation of authigenic carbonates at the seafloor; bubbles or gas hydrates in the sediment (Naudts et al., 2008).

RESULTS AND DISCUSSION

Seismostratigraphic Interpretation

The seismic stratigraphic analysis allowed the reconstruction of the depositional architecture of the stratigraphic units of the late Miocene and Pliocene-Quaternary, as well as the identification of magmatic intrusions. However, due to the lack of boreholes in the study area and adjoining sectors, a precise temporal framework for our seismostratigraphic reconstruction is not achievable. Some major seismic reflections can be assessed with confidence by correlation with CROP line M36, which passes above the volcanic structure E5c (after De Ritis et al., 2019) and crosses several MCS profiles presented in this study (**Figure 2A**).

In addition, a regional reflector associated with the top of the evaporites deposited during the late Messinian Salinity Crisis (MSC) is recognized by analogy with basins in the Western and Central Mediterranean, where it coincides with the top of the trilogy of units of the MSC (Dal Cin et al., 2016; Camerlenghi et al., 2020). The Lower Unit (LU) is inferred to be composed of gypsum and clastics, but is not visible in our data due to the poor energy of our source. The Mobile Unit (MU) is mostly a seismically transparent unit characterized by an upper folded boundary corresponding to evaporites filling the basins and onlapping into the lower continental slopes. The Upper Unit (UU) forms a distinct seismic facies, consisting of a package of high-amplitude parallel and continuous reflections, interpreted as

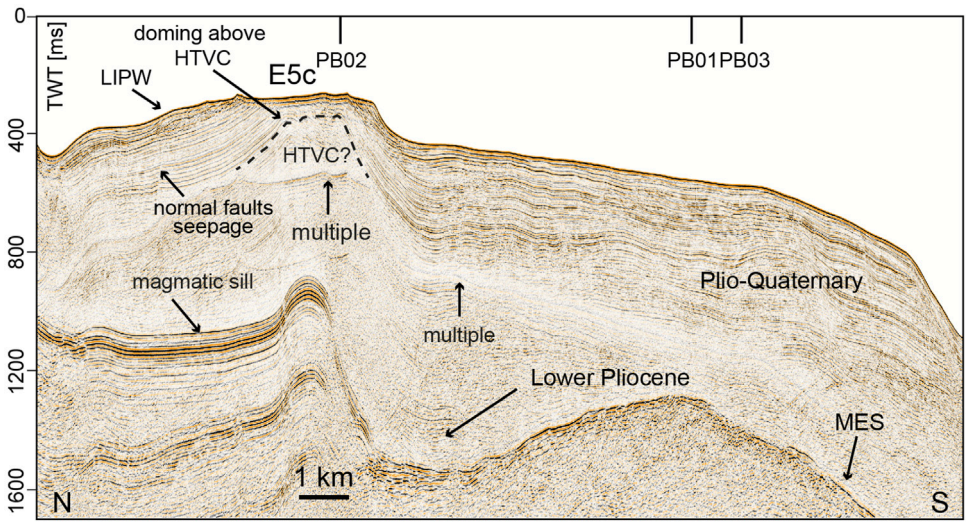

FIGURE 3 | Seismic reflection profile PB12 showing the vertically-stacked magmatic sills and the southward change in seismic facies of the upper Messinian units (MES). Location in **Figure 2A**.

an alternation of anhydrite or gypsum and marl layers. The erosion of these latter two units can be marked by the Margin Erosion Surface (MES), which is widespread on the continental slope of the Western Sardinian margin, where Messinian units are generally absent (Geletti et al., 2014). The MES can correspond with the regional M reflector recognized as the top of the Messinian units or regional unconformity in the Tyrrhenian Sea (e.g., De Ritis et al., 2019). This reflector is often located below the maximum penetration of our MCS data (e.g., **Figure 3**) and its depth surface has been mapped mostly with vintage sparker data (**Figure 2B**).

The overlaying Plio-Quaternary sedimentary succession is characterized by layered, mostly continuous, medium-to high-frequency and moderate to high-amplitude reflections. The Lower Pliocene is generally characterized by semi-transparent reflections (**Figure 3**).

In the northern study area a seismic facies characterized, internally, by high frequency and variable amplitude reflectors with sigmoid external geometry interpreted as "Lowstand Infralittoral Prograding Wedge" (LIPW) formed during pre-Last Glacial Maximum relative sea level lowstands has been identified by analogy with De Ritis et al. (2019) (**Figures 3**, **4A**).

Volcanic seismic features exhibit a mound-shaped or an eye-shaped geometry, with a flat base and convex top, discontinuous and chaotic internal reflectors, which can be interpreted as laccoliths and magmatic intrusions reaching the sea floor. Volcanic chimneys and seepage of fluids along vertical faults are widespread in the shallower sediments (**Figure 4A**). Similarly to the laccoliths, they are confined in the northernmost part of the Paola Basin, indicating that the ascent of magma wanes moving away from the northern volcanic-bearing sector of the study area.

The interpretation of magmatic sills is a problematic task in our data. In particular, the acoustic imaging of sills and the distinction between repeated sills and multiples beneath the first high amplitude sill reflection event (**Figure 3**) is challenging. However, the presence of sills is envisaged at this site in the lower-resolution CROP M36 line, on which, the same feature is interpreted as a magmatic sill associated with a conduit (see **Figure 4** in De Ritis et al., 2019). It is however, noteworthy to say that the seismic facies and striking folding of the reflectors corresponding with the magmatic sill are reminiscent of the acoustic response of the Messinian UU. In the Western Sardinia margin, the Messinian UU can be intercalated by (salt) lenses characterized by a more transparent facies (Geletti et al., 2014), with an overall seismic facies similar to what we observe in our case study (**Figure 3**). However, the presence of the Messinian UU in the upper and mid slope of the study area, where only marginal evaporites consisting of gypsum are believed to be present (Bertoni and Cartwright, 2015), is here considered unlikely. Additional high-resolution seismic data would be necessary to investigate this possible occurrence. Other sheet-like reflections characterized by high-amplitude that cross-cut the host-rock strata may be interpreted as sill remnants, severely disrupted or eroded by the observed diapirism of Messinian or pre-Messinian units (**Figure 4B**). Chaotic reflections and seismic attenuation stem from the sill and form a large vertical conduit below a 1.5 km wide eye-shaped feature characterized by an inner chaotic seismic facies with an external wall, which cuts surrounding clear reflections (**Figure 4A**). Bright spots are visible downslope from the conical edifice of Ov1, that overall can be interpreted as a volcanic feature (**Figure 4C**).

Proceeding farther south, in the non-volcanic sector of the study area, doming and diapirism of sediment below the MES reflector of the Messinian units remain significant (**Figure 2B**). In correspondence of the mound structure R1MV, the diapir gives rise to a prominent conduit which reaches 50 m below the seabed (**Figure 5A**), where bright spots and chimneys are connected to the presence of free gas in the shallow sediment (**Figure 5C**). The small chimney ascending to the seabed is barely visible also in the CHIRP profile (**Figure 5D**). Mass-transport deposits (MTDs) are

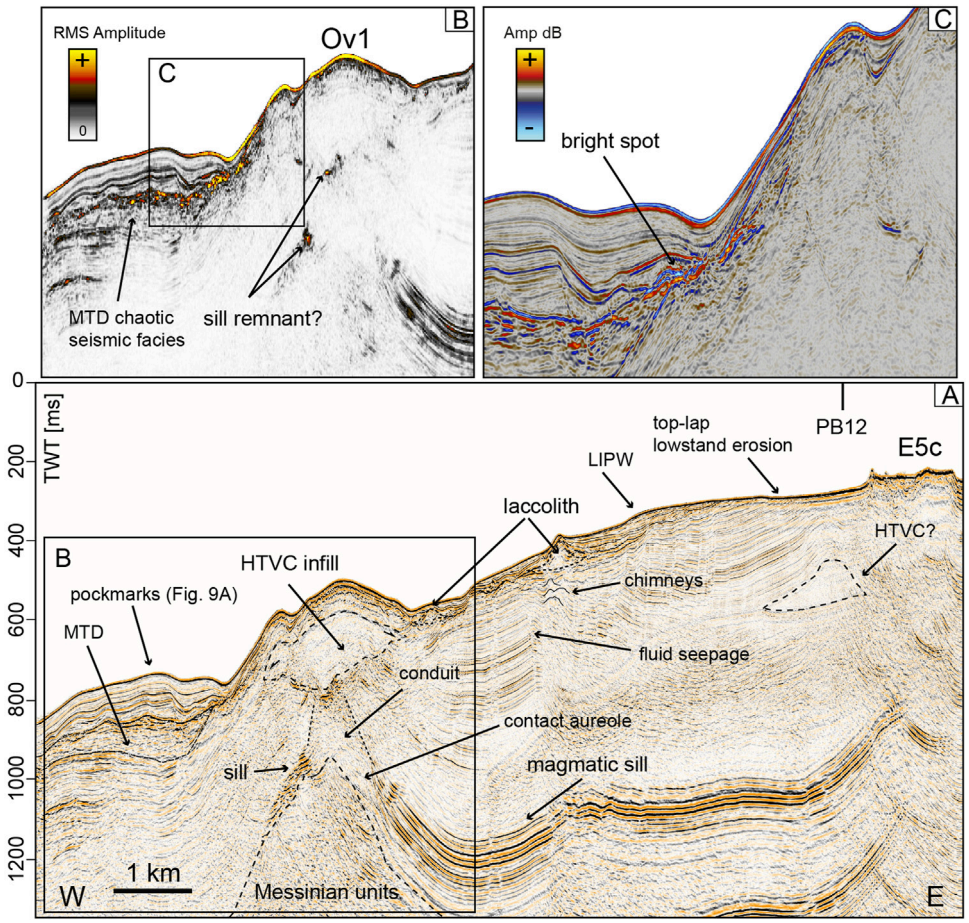

FIGURE 4 | (A) Seismic reflection profile PB02 showing the volcanic edifices of Ov1 and E5c with the hydrothermal vent complex (HTVC) located below Ov1 and the inferred extinct HTVC below E5c. The diapirism of Messinian units is also traced highlighting a conduit feeding the HTVC. Base and top of an MTD located downslope of Ov1 are outlined. **(B)** RMS Iterative amplitude extracted from the profile portion outlined in **(A)** showing possible remnants of a magmatic sill and the MTD chaotic facies. **(C)** Close-up of the seismic line outlined in **(B)**, where bright spots are indicated. Location in **Figure 2A**.

located both at the seabed (**Figure 5D**) and 130 m below the seafloor along the western slope of the mound structure (**Figure 5B**) suggesting a repeating pattern of discharge. A chimney is visible ascending from the top of the MTD, suggesting that gas-charged sediment is present within the MTD, although the latter appears to be sealed by positive amplitude anomalies, indicative of harder material (**Figure 5B**). Plio-Quaternary reflections pinch out against the diapir walls but are disrupted by crater-like reflections followed upward by chimney-like reflections (**Figure 5A**). Locally, the diapirism and associated conduits can reach to the seabed where the high amplitude reflectors are directly connected to the seabed (**Figure 6A**), and where acoustic flares have been detected in the MBES water column data. Sill remnants are possibly present also at these locations (**Figures 5A**, **6B**), while bright spots are quite evident (**Figure 6C**), also in the unfiltered shot gathers (**Figure 6D**).

Farther south, the depth of MES is always below the maximum penetration of our MCS data, however, the isobaths map highlights that the MES is shallower (**Figure 2B**) in correspondence of two mounded structures of very low relief (**Figure 7A**). Seismic attenuation is pervasive below scattered through-over-peak reflections that correspond to an impedance acoustic contrast, evidence of a harder layer located 150–160 m below the seabed (**Figure 7B**). Where these positive anomalies are more continuous, pockmarks are not present at the seafloor. The mound structures are not connected with gas flares in the water column, but are characterized by pockmarks and a crater on the seafloor (**Figure 7B**). Bright spots are present, but are buried below 25–50 m of sediment (**Figure 7C**). A saucer-shape reflection, that may resemble a magmatic sill, is present in the lower part of the Plio-Quaternary (**Figure 7A**).

In correspondence of the mound structure RMV, where the highest gas flare has been recorded, acoustic blanking is relevant (**Figure 8A**), while below the MMV structure a diapiric-like feature is imaged especially by RMS amplitude (**Figure 8B**). Acoustic blanking predominates where the acoustic impedance contrast likely indicates the presence of layers comprised of harder material (**Figure 8B**). Here, the observed scattered positive anomalies (**Figure 8D**) and pull-up events

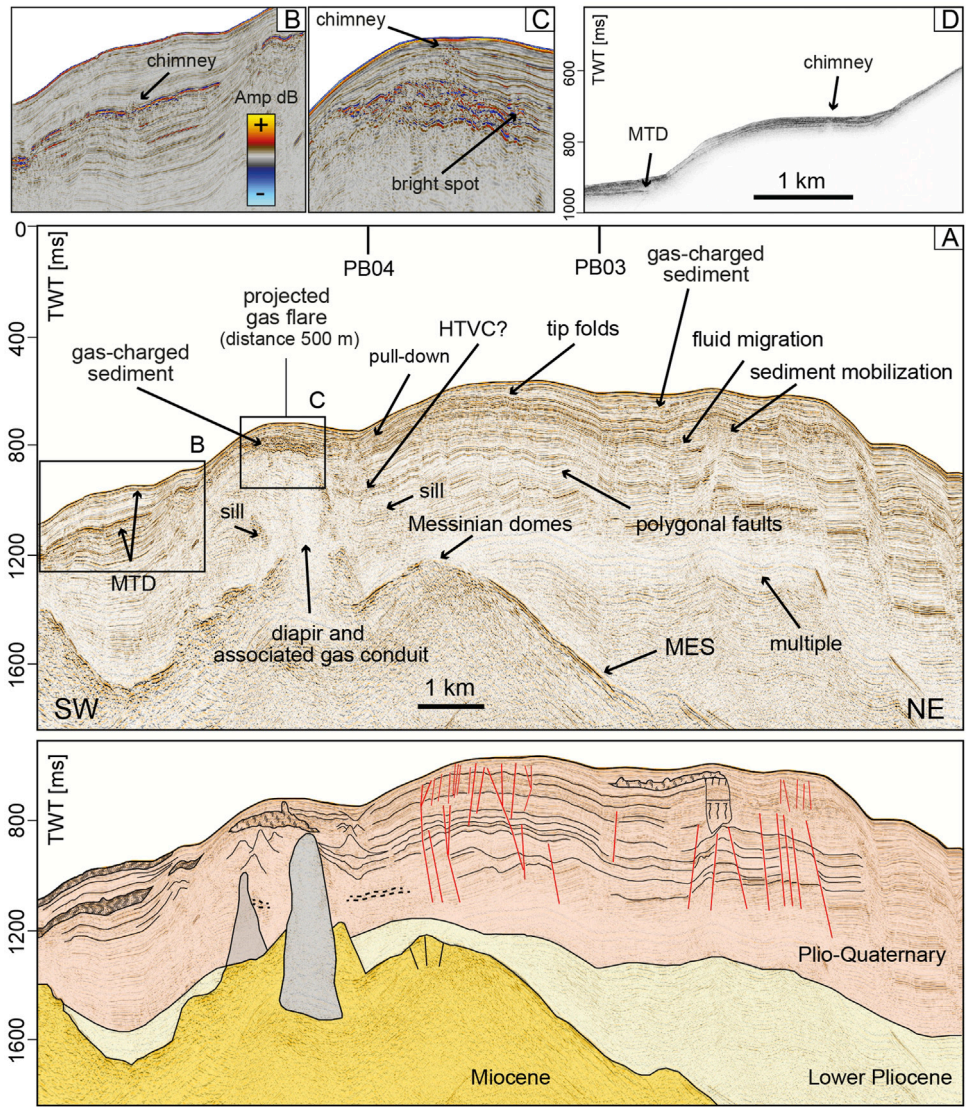

FIGURE 5 | (A) Seismic reflection profile PB01 and its line drawing (lower panel), showing the diapirism of the Messinian units below a projected gas flare in the water column. Close-up panels of seismics showing: **(B)** a chimney above an MTD; **(C)** a chimney emanating from bright spots located 50 m below the seabed. **(D)** CHIRP seismic profile showing the high amplitude character of the shallow reflections, a gas chimney and a shallow-seated MTD. Locations in **Figure 2A**.

(**Figure 8A**) are probably connected with the methane-derived carbonates that were actually collected by sediment coring. Bright spots are located near the seafloor where the gas flares are present (**Figures 8C,E**); in the mound structure where no flares were detected (same of **Figure 7A**) the bright spots are just 10 m below the seafloor (**Figure 8D**). In correspondence of MMV, faults radiate at the summit of the diapiric conduit outlined by seismic attenuation (**Figure 8C**).

Subsurface Gas Indications

Due to increased impedance contrasts, resulting from enriched free gas content in the pore-space, gas in the subsurface becomes visible in CHIRP profiles as enhanced reflectors resulting in high amplitudes of the seabed reflector and few meters below and acoustic blanking underneath (**Figure 5D**). A map of these areas of enhanced high-amplitude in the shallow sediment succession (1–10 m below the seabed) is shown in **Figures 9B**, **11B**. Mapping of high-amplitude reflections indicates that their occurrence is concentrated in the southern sector, around MMV and RMV, suggesting that these areas are influenced by higher gas concentrations. Subsurface acoustic blanking in CHIRP profiles is observed also as few-meters wide vertical chimneys reaching within 3–4 m from the seafloor (**Figure 5D**). Since they correspond with gas flares in the water column, or their projection at distances <500 m, and correlate with similar features in MCS data (**Figure 5B**), they are interpreted as gas pockets. Another type of high amplitude reflections, consisting of narrow vertical lineations, a few meters long, is frequently

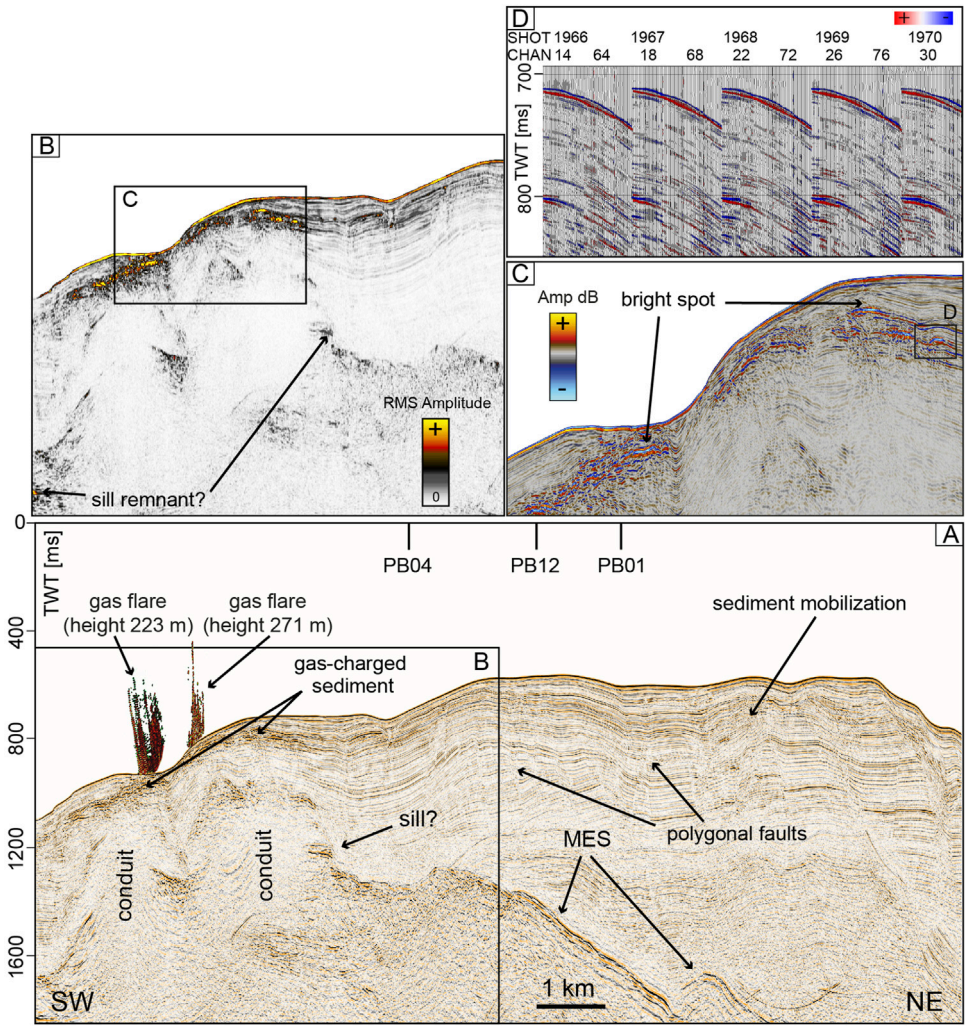

FIGURE 6 | (A) Seismic reflection profile PB03 showing diapirism and conduits below two gas flares in the water column. **(B)** RMS Iterative amplitude extracted from the profile portion outlined in **(A)** and showing bright spots, and possible remnants of a magmatic sill. **(C)** Inset outlined in **(B)** where bright spots are indicated. **(D)** 5 consecutive shot records along profile PB03 at trace 2,739 and 800 ms where a bright spot is present. A large ormsby band pass filter (10–20/500–1,000 Hz) was applied to remove the background noise. Location in **Figure 2A**.

observed close to the seafloor and connects gas chimneys with flares in the water column (vertical bright spots) (**Figures 9A**, **11A**). Vertical bright spots mostly corresponds with areas of pervasive landslide headwall scars (**Figure 9A**) in the northern sector of the study area, or pockmarks in the southern sector (**Figure 11A**).

Gas Flare Occurrence

Gas emissions were detected and identified as flares in water column echograms of the MBES. Due to the limited coverage of the swath needed for water column observations, the total area covered for water column flare imaging by swath coverage was restricted to 2,476 km^2 (**Figure 2A**). These data were loaded in the QPS Fledermaus Midwater tool using the stacked view as initial guide for possible venting, and the fan-view for detailed detection of gas emissions (**Figures 9D**, **11D**). When a flare was identified, its acoustic signal was traced to the seafloor through subsequent fan-images and its geographic location was picked at the central point. The MBES data allow also defining flare locations when offset from the central ship track. However, in this case, identifying the outlet at the seafloor can be problematic due to background noise, especially when flares are not standing out clearly above the seafloor and weather conditions are not ideal. Depending on water depths, bubble size distribution, bubble rise rates, and possible turbulent flows, some frequencies may be better suited for detecting gas in the water column, and EM302 30 kHz acoustic data were the most efficient to detect the gas flares.

In total, 15 water column anomalies were recorded in the study area (**Table 1**). This represents a minimum value, since some distinct flares may appear clustered because their spacing is smaller than half of the MBES footprint used to detect the

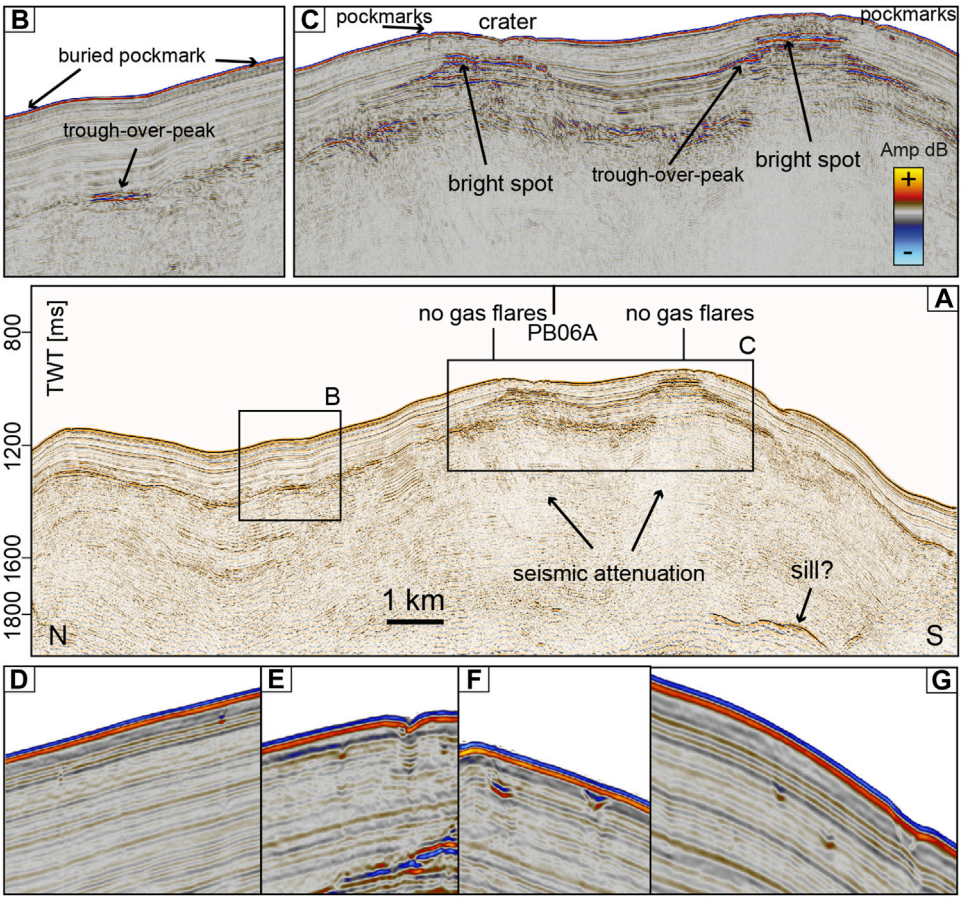

FIGURE 7 | (A) Seismic reflection profile PB04 crossing the area between RMV and MMV and showing seismic attenuation underneath bright spots and scattered trough-over-peak events located 100–150 m below the seabed. Close-up panels of seismics in correspondence of: **(B)** trough-over-peak events; **(C)** bright posts connected with the presence of pockmarks and free gas few meters below the seabed. Location in **Figure 2A**. **(D–G)** Examples of buried pockmarks.

flares (**Figure 9D**). Flare observations were classified according to their appearance being certainly caused by gas bubble emissions. Relatively weak anomalies or with shapes, deviant from a continuous linear feature connected to the seafloor, were therefore discarded; however, their number was negligible compared to the columnar shapes. So far manual identification and extraction, with quality check on, is the common methodology used (Römer et al., 2021), although some attempts for automation have been achieved to distinguish gas flares from fish schools (Minelli et al., 2021). However, the study area is not renowned for fishing grounds, therefore the occurrence of fish schools was unlikely or very limited. As some areas were studied multiple times, flare observations were partly repeated and flare numbers have been corrected for double counting. Double detection during different survey times suggests that most flares are spatially and temporally stable, this is further constrained by the observation of the same flare, characterized by similar height, recorded at RMV in 2011 (Rovere et al., 2014) and 2014 (this study).

Flares were detected at seafloor depths of 548–862 m. Flares appear in heights from less than 20 m in the outlets surrounding the main flares and end mostly within the water column, the only exception being the two flares identified on top of RMV that reach very shallow water depths. Flare height determination is generally limited by the swath geometry, and the upper parts of the highest flares detected at RMV are probably cut off about 15–25 m below the sea surface (**Figure 11D**). However, no natural ebullition at the sea surface was observed during the surveys and there is no reason to suggest that gas exchange with the atmosphere is active at least in calm weather conditions and during the summer season, when both the 2011 and the 2014 surveys have been conducted (August and June).

The flares are always located directly above bright spots and stacked bright spots connected to the seabed or very close to it in the MCS profiles (**Figures 6**, **8**).

Seafloor Morphology and Backscatter in Relation to Gas Flares

Bathymetric mapping of the study area revealed that flare locations are systematically related to specific morphological seafloor elements (e.g., mounds, pockmarks, and linear scarps)

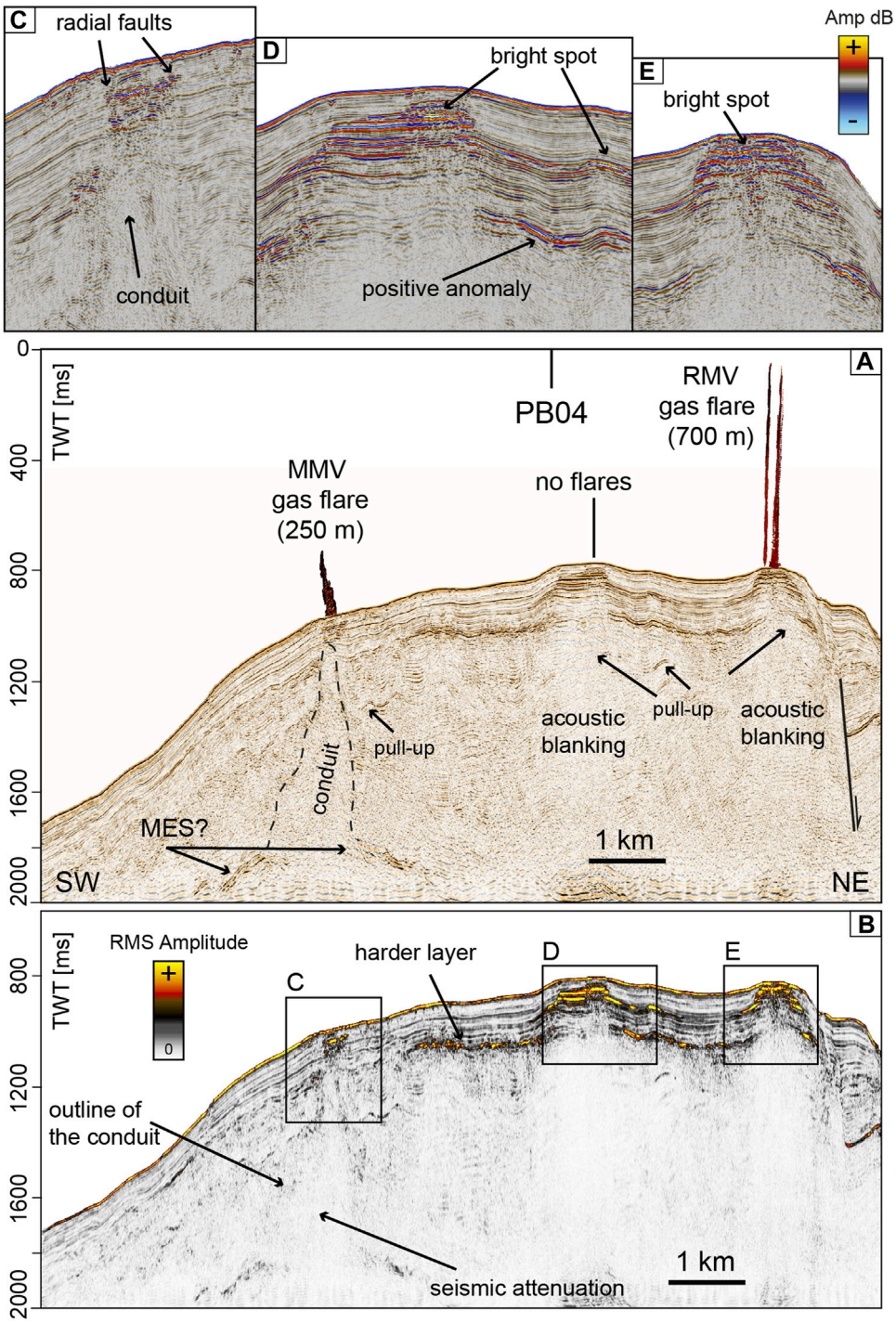

FIGURE 8 | (A) Seismic reflection profile PB06A passing above RMV and MMV where gas flares have been detected. **(B)** RMS Iterative amplitude extracted from the whole profile highlighting a continuous reflection connected to an impedance acoustic contrast due to a harder layer located 100–150 m below the seabed. Close-up panels of seismic in correspondence of: **(C)** MMV; **(D)** the mounded structure not connected to gas flares; **(E)** RMV. Location in **Figure 2A**.

(**Figures 9A**,C, **11A**,C) or seafloor backscatter anomalies (methane-derived carbonate precipitation and fluidized mud at the seafloor) that are usually associated with gas seepage (**Figures 9B**, **11B**). The flares align almost N–S along the seaward slope of the Paola Ridge (**Figure 2A**), the only exception being the flares in correspondence of the RMV. This mound structure is located more landward and is confined by a NE-dipping normal fault, which uplifts the mound with respects to the adjoining Propeller

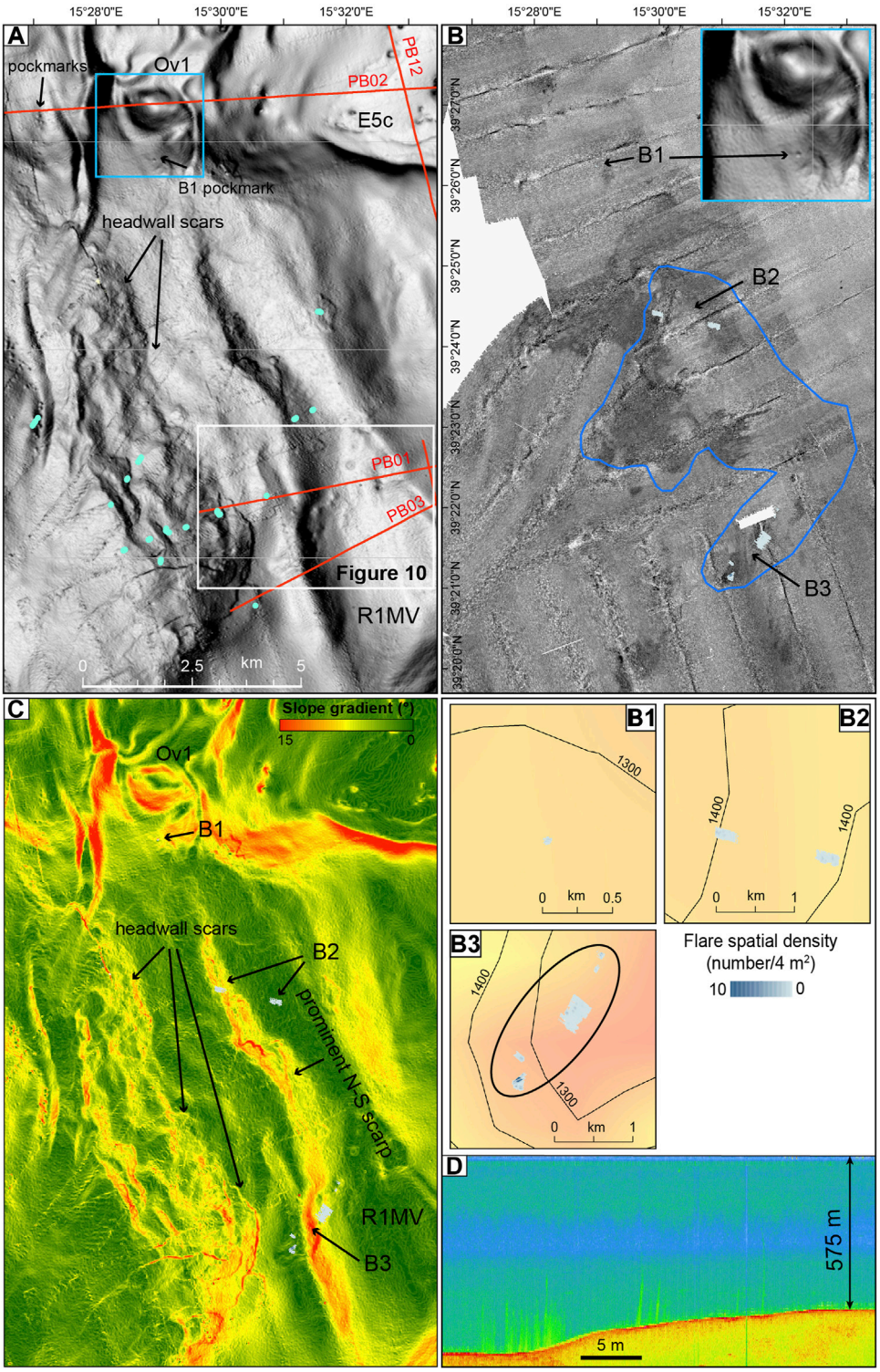

FIGURE 9 | (A) High-resolution MBES bathymetry of the northern sector of the study area with track lines of the MCS data (red), vertical bright spots identified in CHIRP profiles (small baby-blue circles). **(B)** MBES backscatter of the seafloor, the area of shallow high-amplitude reflectors in CHIRP profiles is outlined in blue. **(B1–B3)** are enlargements of flare density superimposed to the depth of the Messinian reflector. Zoom in of the pockmark located on the southern flank of Ov1 is framed in the upper right corner. **(C)** Slope gradient calculated from the MBES bathymetry showing the presence of headwall scars and the N–S scarp connecting Ov1 with the areas of R1MV flares. **(D)** Stacked view of gas flares detected in the water column by the MBES EM302 corresponding with the ellipsis in **(B3)**. The area is outlined in **Figure 2B**.

TABLE 1 | Summary of location, height and water depth at which the flares have been identified in MBES water column echograms.

Location	Structure	Water depth range (m)	Area of plume (m^2)	Max height (m)	Isolated plume	Cluster of plumes	Impacted area (km^2)
northern sector	Volcanic Flank	548	1968	154	Yes		
	Continental Slope	561–629	40,514	227		Yes	0.75
			37,312	238		Yes	
	R1MV	575–706	4,164	297	Yes		1.7
			3,445	90	Yes		
			106,,261	205		Yes	
			10,454	177	Yes		
			16,041	271		Yes	
			8,458	223		Yes	
southern sector	MMV	813–862	9,586	246	Yes		0.2
			9,937	146	Yes		
			17,217	115		Yes	
			27,854	145	Yes		
	RMV	722–736	28,868	597			0.08
			45,905	696			

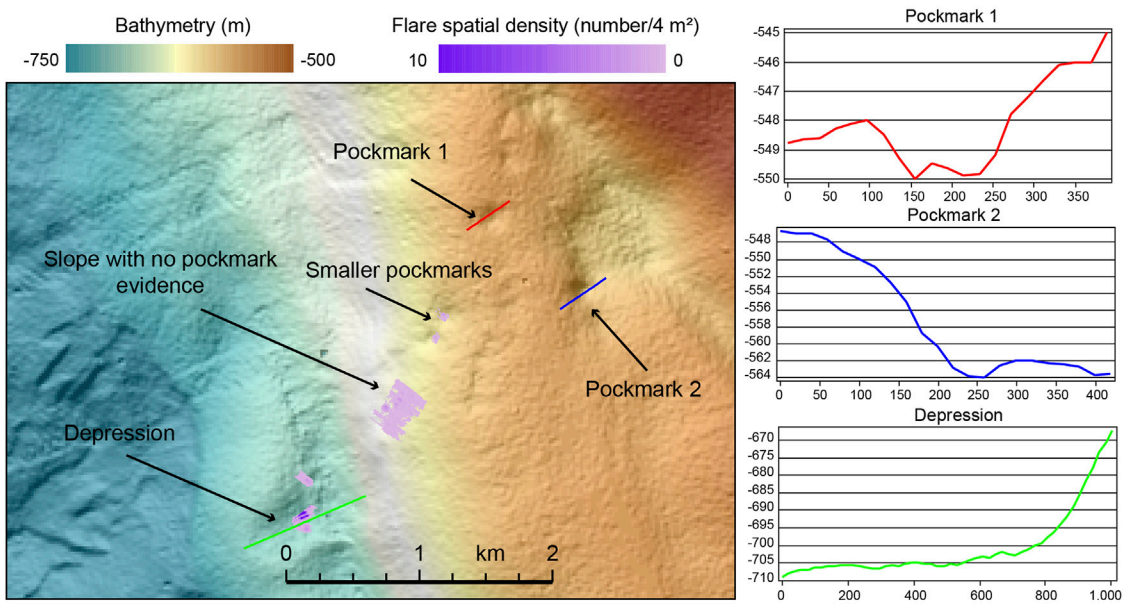

FIGURE 10 | Zoom in of the area of pockmarks and gas flares outlined in white in **Figure 9A**. On the right, bathymetric profiles of larger pockmarks, where no gas flares have been detected, and of the depression where gas flares are more concentrated. Note that flares are located above smaller pockmarks.

Basin (**Figure 8A**) and is particularly evident to the north (**Figure 13**).

The northernmost isolated flare rises above a pockmark located on the southern steepest flank (7–10° gradient slope) of Ov1, a 100-m-high almost conical mound which may be interpreted as an HTVC (**Table 1**, **Figure 9B1**). A sediment core collected on top of Ov1 recovered less than 1 meter of sediment, consisting of conglomerates and carbonate hardgrounds. On the western flank of Ov1, pockmarks are present but limited in number (**Figure 9A**), the largest being 100 m wide, and are probably related to fluid seepage through fractures from the buried MTDs located downslope (**Figure 4A**). The presence of MTDs characterized by bright spots and chimneys, indicative of the presence of free-gas in the sediment and seepage, may be related to past hydrothermal activity and gas discharge.

Other flares develop along a prominent scarp that connects the Ov1 HTVC with R1MV (**Table 1**), and forms a N–S oriented, 12-km-long feature consisting of a series of structural terraces originating a topographically complex slope sector (**Figures 9A,C**). The tallest flares (223–271 m) develop on a small depression (**Figure 10**), downslope from the scarp that makes up the western flank of R1MV (**Figures 9C, B3**). Here, flares are not obviously associated with pockmarks that are <5 m deep, and

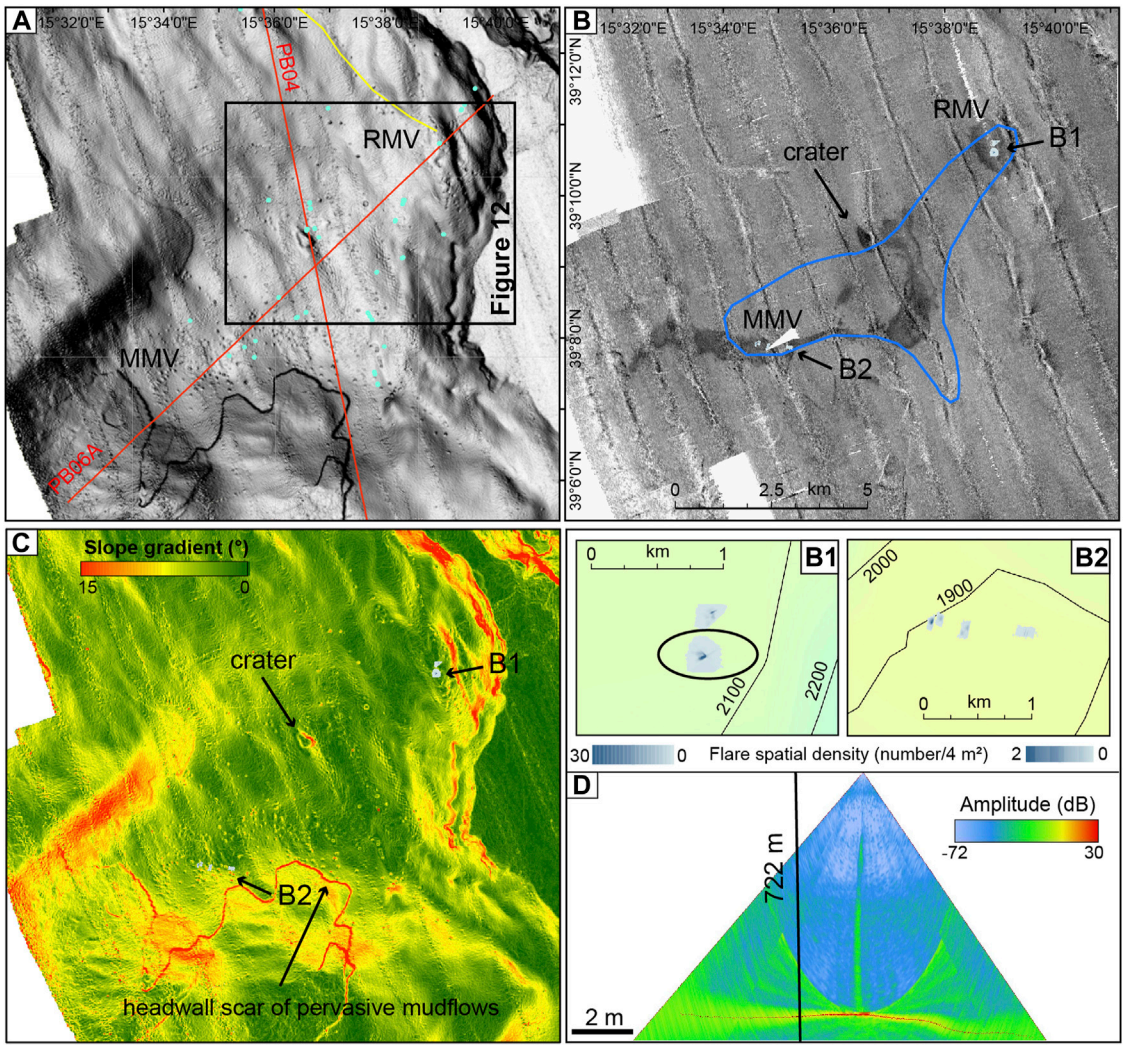

FIGURE 11 | (A) High-resolution MBES bathymetry of the southern sector of the study area with track lines of the MCS data (red), vertical bright spots identified in CHIRP profiles (small baby-blue circles). **(B)** MBES backscatter of the seafloor, the area of shallow high-amplitude reflectors in CHIRP profiles is outlined in blue. **(B1, B2)** are enlargements of flare density above MMV and RMV superimposed to the depth of the Messinian reflector. **(C)** Slope gradient calculated from the MBES bathymetry showing the overall mounded structure comprising MMV and RMV. **(D)** Fan view of the gas flare detected in the water column above RMV by the MBES EM302 corresponding with the ellipsis in **(B1)**. The area is outlined in **Figure 2B**.

averagely 100 m in diameter (**Figure 10**). Flares develop above the smaller pockmarks, a depression and the slope (**Figure 10**).

Gas flares are connected with areas of highest seafloor backscatter and high-amplitude shallow reflections in CHIRP profiles (**Figure 9B**); however, along the northern sector of the study area, the high seafloor backscatter is also indicative of the presence of several landslide headwall scars and erosion at the seafloor that contribute to the character of the acoustic response. Therefore, in this case, the seafloor backscatter is not an exhaustive tool to distinguish areas characterized by fluid seepage and presence of gas on or close to the seabed. Furthermore, a further contribution to the high backscatter can come from the widespread shallow-seated MTDs, possibly related to the discharge of fluidized mud and mudflows from R1MV, as testified by CHIRP profiles (**Figure 5D**). This setting is similar to that of MTDs located downslope of the HTVC of Ov1, where amplitude anomalies are associated with fluidized sediment and gases (**Figure 4C**), and may correspond to eruptive phases, which have now ceased. In addition, the presence of carbonate hardgrounds, in general not associated with active venting (e.g., Svensen et al., 2003), points to the extinction of the main hydrothermal vent activity, on top of Ov1. However, there might be still residual thermal effect reflected by the release of gas through fractures and along the flanks of the edifice.

Moving southward, MMV and RMV sit on a large almost rounded (13.5 × 11.5 km) mound 300 m high. There are no significant morphological differences between MMV and RMV, in terms of height and size, however RMV appears to be fault-controlled. Above MMV, several clusters of gas flares (**Table 1**)

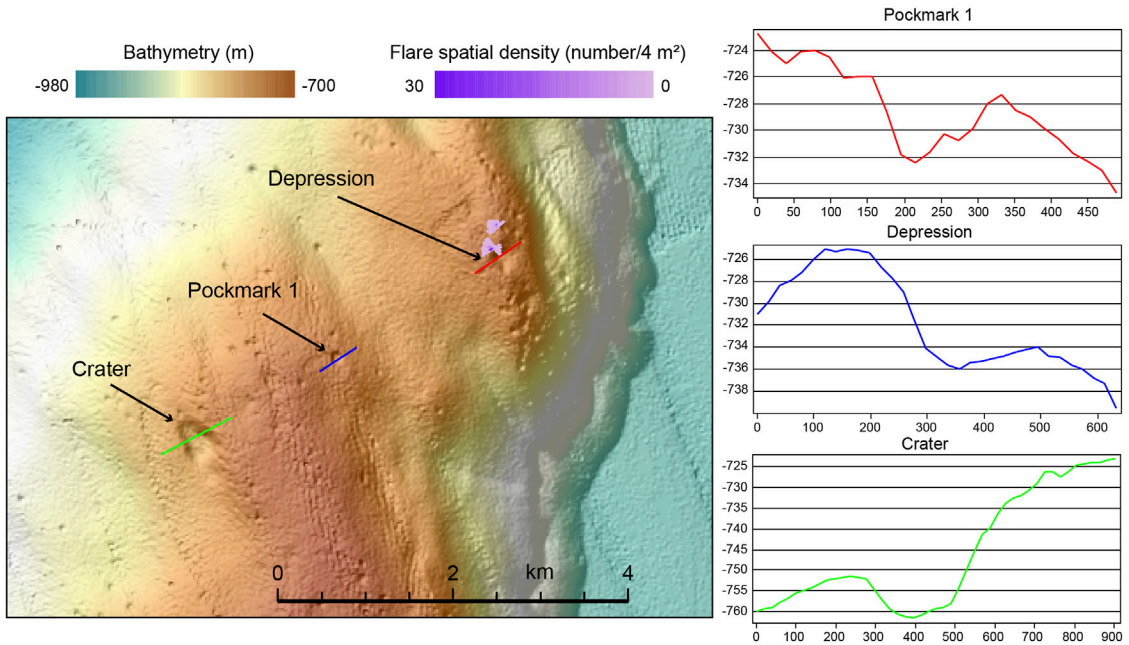

FIGURE 12 | Zoom in of the area of pockmarks and gas flares outlined in black in **Figure 11A**. On the right, bathymetric profiles of an average pockmark and the crater, where no gas flares have been detected, and of the depression where gas flares are more concentrated on top of RMV.

are associated with evenly distributed pockmarks with diameter of about 50 m and average depth of a few meters (**Figures 11A, B2**). The western flank of MMV is characterized by a belt of landslide headwall scars, which might coincide with shallow-seated mudflows (**Figure 11C**). MMV and RMV are morphologically separated by the largest depression observed in the study area. The latter is a 250 m wide and 10 m deep, crater hosted in a subtle saddle (< 40 m deep) between MMV and RMV, not associated with any gas flares (**Figures 11A**, C, **12**). On top of RMV the two highest gas flares detected in the study area (700 m against a water column of 736 m) develop above pockmarks and a depression, which has dimensions similar to the crater (**Figure 12**).

Also in the southern sector of the study area, the gas flares always coincide with high seafloor backscatter areas, which are however larger than those affected by gas discharge in the water column. Although slope gradient at the mounds flanks may enhance seafloor reflectivity, the very high backscatter of the crater may be a further evidence of the presence of gas in the first 25–50 m of the sub-seabed. This is further supported by bright spots in MCS data (**Figure 7C**), that may be related with a past outburst that formed the crater.

In other seep areas, steeper dipping and higher mounds are indicative of recent or prolonged growth of structures, whereas, lower-relief and gentler topography are associated with older features (e.g., Serié et al., 2012). In the study area, the differences in the morphology of the mounds are not so significant, and therefore may not be indicative of their different development stages and seepage activity. Furthermore, the seafloor reflector does not show significant variations in seismic amplitude with depth and topography, suggesting that the seafloor is everywhere covered by the same type of sediment, with the only exception coinciding with the erosional seafloor downslope R1MV.

Dissolved Gases in the Water Column and Bottom Waters

Gas samples from two box-cores collected on RMV (flare B1) and R1MV (flare B3) revealed a chemical composition dominated by CO_2 (up to 98.73% by vol.) and subordinately by N_2 (up to 1.26% by vol.) and methane (< 0.06% by vol.). The carbon and oxygen isotopic ratios of CO_2 are −1.8 and −1.1 (V-PDB ‰) and −2.4 and −4.4 (V-PDB ‰), respectively. Data collected with the Niskin bottles carry negligible CH_4 and other hydrocarbon content, probably due to the difficulty in controlling the lowering of the rosette sampler inside the flares and reaching close to the bottom. The chemical composition of the Niskin samples is similar to present-day seawater, whereas the alkalinity is slightly higher (Franchi et al., 2017).

Spatial Distribution of Flares in Relation with Diapirs, Faults, Magmatic Sills and Mineral Deposition

All flares detected are found in correspondence of subsurface of diapirs apparently originating from upward folding of the top Messinian units and diapirism connected to gas conduits directed to the seabed. The highest abundance of flares occurs around the diapir observed below R1MV (**Figure 6A**), while the highest gas flares were detected in connection with acoustic blanking

connected with up warping of the Messinian units (not imaged by our MCS data) below RMV and doming and diapirism below MMV (**Figure 8A**).

Gas chimneys or conduits, that represent the path of vertically migrating gas into shallow reservoir sediments below bright spots, and that are located above salt domes has been detected in various geological contexts, such as: the German North Sea (Müller et al., 2018); the upper continental slope of the Santos Basin offshore Brazil (de Mahiques et al., 2017), where Miocene diapirs are associated with fields of pockmarks on the seabed; the Angola offshore (Serié et al., 2012), where a cluster of gas hydrate pingoes is attributed to a gas migration system along the flanks of a salt diapir. In the Mediterranean Basin, Messinian evaporites deposited in thick sedimentary successions in the deepest sub-basin depocenters as a consequence of the MSC. Although salt diapirs and domes are normally implicated in shaping the thermal and dynamic fluid circulation and seepage, this straightforward relationships is not always observed in the Mediterranean. In the Nile deep-sea fan, not all mud volcanoes are linked to the presence of thick Messinian evaporites (Bertoni and Cartwright, 2015). Even in the Levantine Basin, diapirism of Messinian salt and focused fluid flow reaching the seabed in the form of chimneys, which cross the thick basinal Messinian evaporites and originate in the pre-Messinian units, are not directly linked with mud volcanoes (Hübscher et al., 2009; Bowman, 2011). In the Western Mediterranean, the largest Messinian diapiric structures form in the Plio-Quaternary depocentres, where the sediment overburden is larger (Geletti et al., 2014) and the buoyancy difference between indurated gypsum and overlying soft deep-sea muds favours the initiation of diapirism (Dal Cin et al., 2016). Less frequently, in these deep basins, salt diapirs cause intense deformation in the upper Plio-Quaternary, breach through the sea bottom and give rise to prominent surface fluid flow. On the contrary, in the slope context of the study area, where only gypsum deposits are present, which makes quite a different lithological and dissolution pattern compared to halite, diapiric structures concentrate where the thickness of the Plio-Quaternary is reduced in connection with up warping of the MES reflector (**Figures 5A**, **6A**).

Furthermore, in the Western Mediterranean, salt deformation was intense during the Lower Pliocene, whereas in the Paola Basin, a more prolonged phase of up-rising and deformation of the diapiric structures, not necessarily connected with passive diapirism of evaporites, is indicated by pinch-out terminations of the upper Quaternary units (**Figure 5A**). This may be explained with a tectonic control over the emplacement of the diapirism in the Paola Basin, which prevail over sedimentary processes. On the other hand, the presence of massive free gas in the very shallow subsurface and vigorous and steady gas flares in the water column, as above R1MV and RMV, requires high fluid flux which is usually associated with a supply of thermogenic fluids by a deep-rooted plumbing system (e.g., Plaza-Faverola et al., 2015). In our case study, this plumbing system likely exploits normal faults, which are not obviously imaged in our MCS data because of the intense acoustic masking. This notwithstanding, a normal fault along the western boundary of the Propeller Basin is

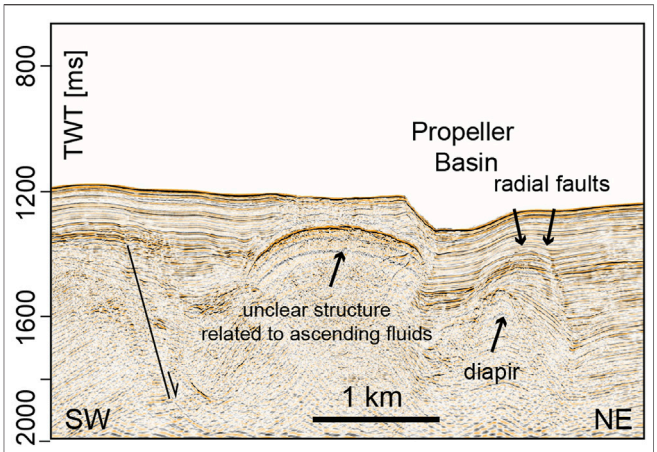

FIGURE 13 | Seismic reflection profile PB07 showing the normal faults that can be traced along the Propeller Basin. Location in **Figure 2A**.

imaged (**Figure 13**). Above the conduits, radial faults are often present, especially on top of MMV (**Figure 8C**). The conduits below R1MV and MMV, that are associated with gas flares in the water column, align along the westward slope of the Paola Ridge which is tectonically controlled by normal faults (Gamberi and Rovere, 2010) and experienced subsidence during Pliocene to Quaternary times (Pepe et al., 2010).

In addition, polygonal faults are observed in the upper Plio-Quaternary to the east of the gas flares area of R1MV, they are related to unfocused fluid flow probably by the early expulsion of pore waters in the fine-grained sediments of the Plio-Quaternary. Only few of these faults have a subtle manifestation at the seafloor, indicating recent activity (**Figure 5A**). In the Western Mediterranean, polygonal faulting directly above the thick stratified evaporite sequence may have formed in response to water release from the underlying evaporites, due to gypsum-anhydrite conversion. The gypsum-anhydrite diagenetic reaction is temperature and depth-dependent (Bertoni and Cartwright, 2015). Therefore, given the relatively shallow-burial depth in the R1MV area, the likely presence of only gypsum in the Messinian units, a high geothermal gradient/heat flow should be invoked for addressing the diffuse fluid seepage along the polygonal faulting area east of R1MV.

The presence of magmatic sills in the Plio-Quaternary succession of the study area (**Figures 4A**, **5A**) may represent the explanation for the additional thermal gradient needed for the observed intense fluid flow and gas venting in connection with up warping of thin Messinian evaporites in the study area. The upward folding of the Messinian units and seal bypass can be therefore associated with fracturing caused by the hot igneous intrusions, that are interconnected or lie just above the sealing succession (**Figures 4A**, **5A**), as in other contexts such as the Rockall Basin in the NE Atlantic (Cartwright et al., 2007). The heating of the colder and wetter Plio-Quaternary sediments may have resulted in boiling of pore water, rapid maturation of organic matter in the sill aureole and overpressure around the sill with the formation of the fracture network along which

gaseous hydrocarbons, water and magmatic material escaped to the seabed and formed eye-shaped or domed HTVCs (**Figure 4A**), where material is extruded into the seafloor and may resemble a mud volcano system (e.g., Iyer et al., 2013; Roelofse et al., 2021).

The assessment of the presence of sills in our MCS data remains problematic, although subtle evidence of magmatic sills may be detected in the lower part of the Plio-Quaternary (**Figures 5A**, **6B**, **7A**). The subtle evidence of magmatic sills may be due to: lack of seismic signal penetration; acoustic masking caused by the transparent facies of the diapirs and gas conduits (**Figure 8A**); fractures that may form for either thermal contraction during cooling, metamorphism in the contact aureole and rapid loss of hydrothermal fluids from the surrounding sediments (e.g., Cartwright et al., 2007; **Figure 4A**).

Seismic acoustic masking has been interpreted as gas chimneys or gas-charged fluid migration conduits also in areas not in connection with salt domes (Plaza-Faverola et al., 2015; Waage et al., 2019). A minor fraction of free gas in the pore space of sediments is sufficient to produce signal blanking in form of chimneys that can be thus regarded as gas-charged fluid migration pathways. On the other hand, acoustic masking and seismic attenuation can be due to the shadow effect by a sharp impedance contrast when short offsets are used in the acquisition of the seismic data, such as in the system used for this study. The acoustic masking zones underneath RMV and the other mounds in the southern sector of the study area crosscut the entire Plio-Quaternary succession (**Figure 7A**). The masking zones are located below scattered high-amplitude positive anomalies located 150–170 m below the seafloor, intercalated with bright spots and seismic pull-up events that may be associated with authigenic minerals (**Figures 6A,B**). This is confirmed by the fact that, where no high-impedance contrast is visible, the conduit rising to the seabed is well imaged by RMS amplitude, such as below MMV (**Figure 8B**). The scattered character of bright spots in the mounds, where no gas flares have been recorded (**Figures 7C**, **8D**), may further suggest that the lower-impedance contrast is caused by gas within the pore space and fractures rather than gas bubbling at the seabed surface. On the contrary, the positive anomalies may be related to the presence of authigenic carbonates or other types of deeper mineralizations that hamper the seepage towards the seabed. The isotopic signature of the authigenic siderites (δ^{13}C 3–10 V-PDB ‰, δ^{18}O 8–9 V-PDB ‰) collected in the sub-seafloor of R1MV, RMV and MMV (< 10 m) indicate a precipitation in the methanogenic zone (Rovere et al., 2015). Therefore, the seep-carbonate horizons may be fed by the migration of thermogenic methane and hydrocarbons from deeper levels below the Messinian units, or by maturation of the organic matter favoured by the thermal anomaly connected to the magmatic sill as, for example, in the Guaymas Basin (e.g., Simoneit et al., 1988). In the area of the crater separating MMV and RMV, where gas flares are absent, a bowl-shaped deep reflection can be interpreted as a magmatic sill connected with the development of HTVCs that are not presently active. Here, fluids migrated through the lower part of the hydrothermal vent complex, which acted as a vertical zone of high-permeability, enhanced fracturing of the host sediment and circulation of fluids. However, the fractures that develop during the initial stages of hydrothermal activity within the metamorphic contact aureole are highly subject to mineralization and clogging by cementation (Cartwright et al., 2007). Therefore, it is here suggested that the majority of the HTVCs in the southern sector of the study area formed in consequence of an initial gas-dominated explosive phase, but soon became inactive due to their pervasive mineralization. The thermal effect continued to promote the maturation of organic matter and deposition of methane-derived siderites that in turn progressively acted as major barrier for fluid seepage to the seafloor (**Figure 7A**). Where gas venting have been observed in the water column, either the hydrothermal activity is still prevalent or precipitation of methane-derived carbonates is not sufficient to prevent prolonged gas migration.

Flares and Hydrothermal Vent Complexes, Geodynamic Implications

Magmatic activity in sedimentary basins has a critical impact on fluid migration as hot intrusive rocks elevate the local geothermal gradient. The main temperature effect of magmatic sills is believed to last only few thousand years (Roelofse et al., 2021). However, normal faulting, which is quite common in hybrid sedimentary-volcanic systems, causes downward displacement of hanging wall sediments that are initially colder. This process results in the thermal instability of the basin, which may regain its steady state only after a long period, in the order of a few millions years (e.g., Sydnes et al., 2019). There are cases, such as the offshore of eastern Australia, where an Eocene phase of magmatism feeding hydrothermal vent complexes has been linked to the formation of buried mud volcanoes and is believed to still influence the occurrence of seep-related features at the seafloor (Rollet et al., 2012). Therefore, we interpret the Paola Basin as a site where magmatic intrusions, which remain challenging to image in our data but are likely present based of numerous linked observations, have provided the necessary thermal gradient to maintain an effective hydrothermal system.

In hybrid sedimentary-volcanic systems, inorganic CO_2 concentrations generally exceed 50 vol%, whereas CH_4 concentrations are generally lower (roughly > 1–2 vol%). Their surface manifestations, like muddy craters or bubbling pools, may be similar to, and thus may be confused with, pure sedimentary gas manifestations (hydrocarbon seeps), such as mud volcanoes (Procesi et al., 2019). According to a global review (Procesi et al., 2019), the δ^{13}C-CO_2 carbon isotope signature, related to decarbonation reactions (thermo-metamorphism) and magma-mantle degassing at high temperatures (> 250°C) varies from −8‰ to +2‰. These values are in agreement with those recorded at the two gas venting sites sampled above R1MV and RMV (−1.8 and −1.1 V-PDB ‰), implying that there must be a contribution from deep magmatic and metamorphic systems to the gas released at the seabed in the Paola Basin, although a certain contamination from seawater CO_2 cannot be excluded in our isotopic signal, due to the sampling of gas bubbles from the box

core. It must be added that the presence of an evaporitic sequence, although thin, such as the top Messinian unit, modifies pressure and temperature regime, adding a forcing to the sediment burial and fluid history of the basin, including complex feedbacks of diagenesis and dissolution. Furthermore, the diapirs originating from the Messinian units are connected through extensional faults to the deep-rooted plumbing systems. This setting enhances fluid migration of both abiotic CH_4, formed by deep magmatic and post-magmatic high-temperature reactions and biotic thermogenic CH_4 related to thermal reactions on organic matter, which is reflected in the precipitation of isotopically heavy carbonates.

The timing of the onset of fluid seepage in the study area must be better constrained. In the Mediterranean area, fluid flow systems formed around the Messinian time, and were sourced from the pre-MSC under saturated fluids and overpressured sediments, below the thick gypsum-halite sequences (Bertoni and Cartwright, 2015). The absence of paleo-pockmarks or limited presence of pockmarks buried by a thin (> 5°m) veneer of sediment (**Figures 7B,D–G**) and evidence of pinch-out terminations against the diapiric structures in the upper Plio-Quaternary sediment (**Figure 5**) point to a post-MSC activity of the seepage in the study area. In general, fluid flow dated after the MSC seems more dependent on the local geodynamic and depositional settings (Bertoni and Cartwright, 2015); therefore, a Pleistocene age would be more coherent with the establishment of magmatism in the area.

As a matter of fact, the geodynamic history of the Tyrrhenian Sea started at 10 Ma with the opening of the basin. The eastward migration and intensification of the rifting, between 10 and 5 Ma as a consequence of the slab roll-back, triggered seafloor spreading in the Vavilov back-arc basin and the formation of subduction-related volcanism. Between 5 and 0.6 Ma, the rifting migrated further to the southeast and seafloor spreading started in the Marsili back-arc basin, with the emplacemeant of oceanic crust (see Malinverno, 2012 and references therein). Around the same time (0.6 Ma), STEP (Subduction-Transform-Edge-Propagator) faults, associated with lateral lithospheric tearing, are believed to have formed (Cocchi et al., 2017; De Ritis et al., 2019) in the eastern Tyrrhenian domain. The STEP faults acted as the main conduit for upwelling of the isotherms due to mantle melts upraising from the edge of the slab along the lithospheric tear. Therefore, these inferred STEP faults would have controlled the magma uprising that fed the Palinuro volcanic complex (west of Glabro, outside of the area depicted in **Figure 1B**) and the Diamante-Enotrio-Ovidio volcanic-intrusive complex (**Figure 1B**). At present, the upwelling of subduction-induced mantle flow has stopped in the Diamante-Enotrio-Ovidio volcanic-intrusive complex, while the subduction-related volcanism continues in the Aeolian Arc (De Ritis et al., 2019). This reconstruction seems compatible with magmatism of Pleistocene age in the area located south of the Ovidio complex, which may have enhanced the fluid circulation in the Paola Basin, in a complex feedback system, including the top of Messinian units.

The hydrothermal vent complexes that develop along the eastern side of the Tyrrhenian domain deserve better understanding. There are indeed striking morphological and geochemical similarities with volcanic-hydrothermal systems located in shallow waters along the margin. For example, the morphology of seabed and nature of the gas is similar to active seabed doming and gas discharge in the Gulf of Naples (**Figure 1A**), where He and CO_2 are sourced from mantle melts and decarbonation reactions of crustal rocks (Passaro et al., 2016). Other large fluid-escape depressions and seafloor mounds have been observed on the continental shelf of the Pontine Archipelago (**Figure 1A**), where hydrothermal sulfides collected on the seabed and sub-seabed point to the possible degassing of magma similar to the one feeding the latest volcanic activity occurred on the islands in the Middle Pleistocene (Conte et al., 2020). Hydrothermal fluids discharged at this location are CO_2-rich and show a mantle-derived signature indicating that cooling magmas are still releasing enough thermal energy to feed an active hydrothermal system (Italiano et al., 2019). An example in water depths closer to our case study, is the fault-controlled system of deep-hydrothermal circulation discovered on the Cape Vaticano Ridge (**Figure 1B**). Here, δ^3He enriched bottom waters are related to magmatic intrusions generated from mantle-wedge partial melting above the Tyrrhenian-Ionian subducting slab and melt upward migration (Loreto et al., 2019). Therefore, submarine hydrothermal systems and vent complexes along the eastern side of the Tyrrhenian domain remain overlooked especially in deeper waters, where geophysical and geochemical data are sparse. The study of surface expressions of fluid circulation, such as near-seabed seepage and fluid discharge in the water column, would enable to better understanding their relationships with the deep processes associated with slab-subduction, slab tearing and mantle-wedge partial melting.

CONCLUSION AND OUTLOOK

Multichannel seismic investigations and detection of the acoustic backscatter of the water column by multibeam systems were carried out jointly in an area of intense gas seepage and venting in the water column, located in the Paola Basin, at the junction between the back-arc extensional domain and the fore-arc of the Calabrian accretionary wedge, in the southeastern Tyrrhenian Sea.

Using a ship-based multibeam echosounder we detected 15 clusters of flares that are indicative for free gas releases from the seafloor, which are mostly related to seafloor pockmarks, landslide headwall scars and fault scarps. The multichannel seismic reflection survey was designed to achieve the highest resolution in the shallower part of the sub-seafloor, where free gas accumulations and seep conduits were the primary target of our investigation. However, the seismics obtained also the imaging of deeper faults and Messinian units, which were already suggested to be related to the deeper-plumbing system of the seeps (Gamberi and Rovere, 2010; Rovere et al., 2014). Flares are related to acoustic blanking in MCS, high-amplitude

reflections in sediment profiler echograms, and high seafloor backscatter/reflectivity, all of which are indicative of pervasive free gas concentrations in the sediments. The results of these surveys allowed to define the depths of the free gas zones, which are located a few meters below the seabed.

Flares are not randomly distributed but show a relation to locations of magmatic sills, subsurface doming and diapirism at the top of the Messinian units. Possible Miocene fault-controlled hydrocarbon plays (and source rocks) are responsible for charging the mounded complexes with free gas through the faulted network and the overlying chimneys and conduits formed by hydrothermal vent complexes fed by magmatic sills intruded within the Plio-Quaternary deposits. Naturally seeping gas reaches the seafloor along sub-vertical faults, which have formed concurrently or soon after the establishment of diapirism. The main phase of magmatism occurred in the Pleistocene but fluid flow is a long-term process that continues after cessation of magmatism. Geochemical analysis of the dissolved gas, performed at the sea surface, confirm a deep, metamorphic origin of the gas, possibly provided by the magmatic and intrusive complexes surrounding the Paola Basin.

The transient nature of seepage or its absence must be better investigated with repeated surveys with the same acoustical tools, and validation of the acoustically defined features with *in-situ* measurements. The fact that gas flares are not ubiquitous above the sub-surface diapirs and small shallow sediment chimneys may indicate that the absence of water column anomalies is not fixed in time. A thicker seal of sediment and layers of hydrocarbon seep-related methane-derived carbonates may hinder gas release at specific locations, being the evidence that explosive hydrothermal activity, which released large quantities of gas and formed craters at the seafloor, may have ceased in the recent past (few thousand years ago).

Additional sampling of gas is further required because very little is known about long-term variations in the gas flux and venting over days to weeks and months, seasonal cycles and decades. The variability of gas fluxes might be controlled not only by fluid flow rates mediated by microbial processes but also by physical changes in bottom pressure in connection with tides, bottom currents, storms, swell, or earthquakes (e.g. Riedel et al., 2018). Furthermore, varying temperature within reasonable limits at flare sites may change the flow-rate by up to 5% and we only have data from two surveys carried out during the summer season. At the very least, despite our study did not systematically investigate the temporal variability, current observations do indicate that flares are stable over times of hours and days.

More importantly, targeted gas samplings, at the seafloor pressure conditions, and further analysis such as isotopic ratios of helium, carbon, and $^{4}He/^{20}Ne$ are required to unravel the true nature of the fluids released from the seafloor. A certain dissolution of CH_4 in the water column (700–800˚m) is expected, since the vertical transport of dissolved methane is highly restricted by the density stratification of the water column and strong summer thermoclines can limit the vertical gaseous transport. At least on continental shelves, summer thermoclines have been demonstrated to constrain methane transport to the mixed layer and the atmosphere (Schneider et al., 2011). Therefore, gas exchange leads to fast dissolution of methane out of the bubbles during their ascent in the water column. How much methane is released in form of gas bubbles and dissolved in pore water from the seafloor can be overlooked due to the sampling method used in this survey. Dedicated sampling efforts with ROVs, calibration of the acoustic methods with *in situ* flow measurements, and repeated imaging of the same regions during different tides, seasons and years are therefore necessary to assessing flow-rates in the study area.

Some hydroacoustic flares were observed to reach close to the sea surface, thus part of the released gas through seepage may contribute to the atmospheric inventory, but this has to be confirmed by further investigations. Seeps slowly release hydrogen sulfide, methane and other hydrocarbon-rich fluids in the water column, however uncertainties remain regarding the quantity of free methane that is emitted from deep-water seeps into the water column, with several authors showing that, at least in gas hydrates scenarios, most of the methane emitted per year within the gas hydrate stability zone remains trapped in the deep ocean (Römer et al., 2012). In our hybrid volcanic-sedimentary case scenario where fast venting of possible mixed hydrothermal and hydrocarbon gases is observed, a first qualitative assessment of the gas released, even if not constrained in terms of quantities, provide a possible case study for the release of greenhouse gases into the atmosphere. Long-term monitoring and repeated observations also at the sea surface to detect localized exchange with the atmosphere would allow for evaluation of the variability of gas emissions and provide evidence for the controlling mechanisms in our study area.

In summary, understanding the geographical distribution of gas venting sites along the eastern Tyrrhenian continental margin, constraining better their relation with the thickness and facies of Messinian units, hydrocarbon seeps, magmatic intrusions and hydrothermal vent complexes fed by mantle melting and monitoring their long-term variability are key to unravel the feedbacks of the sedimentary, tectonic and volcanic processes occurring at the margin. In addition, hydrocarbon formation and oceanographic processes that influence the distribution and burial of organic matter deposited on the seabed are important controlling factors that must be studied in more detail also for petroleum prospecting targets. Magmatic activity in sedimentary basins may indeed turn an otherwise unprospective area into a geothermal energy and hydrocarbon field (Roelofse et al., 2021). The igneous activity may have induced seal bypass systems, by breaching the Miocene regional seal across the study area and may have enhanced late-stage hydrocarbon generation and expulsion, with the formation of unconventional reservoirs.

DATA AVAILABILITY STATEMENT

The multibeam datasets generated for this study can be found in the bathymetry viewing and download service at https://portal.emodnet-bathymetry.eu/ of EMODnet Digital Bathymetry (DTM). https://doi.org/10.12770/bb6a87dd-e579-4036-abe1-e649cea9881a. Multichannel seismic data and water column echograms can be made available upon request to the corresponding author. The Institute of Marine Sciences of the National Research Council in Bologna (http://www.ismar.cnr.it/) can be enquired for accessing the digitalization of the Sparker database (SDB) at responsabile@bo.ismar.cnr.it.

AUTHOR CONTRIBUTIONS

MR provided funding acquisition as well as cruise preparation and management for R/V Urania cruise Marbeep 2014. MR, AM, and FG carried out on board hydroacoustic data collection, sediment and water sampling. AM took care about the hydroacoustic data processing, curation, and archiving. FZ acquired and processed MCS data. MR interpreted the hydroacoustic and MCS data. All authors contributed to the interpretation of the overall results. MR took the lead in writing the manuscript.

FUNDING

This research was funded by the Ritmare Project (www.ritmare.it), SP4 WP1 AZ3, including open access fees.

ACKNOWLEDGMENTS

We warmly thank the crew of the R/V Urania and the scientific party on board the MarBeep 2014 campaign for their contribution to the success of the cruise. Scientific party: MR (chief-party), FG (co-chief), Elisa Leidi, AM (navigation), Andrea Gallerani, Fabio Savelli (sediment sampling), FZ, Lorenzo Sormani, Lorenzo Facchin, Gianpaolo Visnovic (multichannel seismic acquisition), Bruna Petani, Eugenio Rastelli, Andrea Fioretti (biological sampling), Heba Rashed, Luciano Giannini, Yuri Galletti (water sampling), Fabio Canziani, Filippo Villi (trainees). We are also grateful to the Institute of Marine Sciences of the National Research Council in Bologna, Italy (http://www.ismar.cnr.it/), for providing and making accessible the digitalization of the Sparker database (SDB) comprising BP profiles. Filomena Loreto and Valentina Ferrante are particularly thanked for inspiring the initiative. Schlumberger and University of Bologna are thanked for the provision of Petrel software.

REFERENCES

Berndt, C., Hensen, C., Mortera-Gutierrez, C., Sarkar, S., Geilert, S., Schmidt, M., et al. (2016). Rifting under Steam-How Rift Magmatism Triggers Methane Venting from Sedimentary Basins. *Geology* 44, 767–770. doi:10.1130/G38049.1

Bertoni, C., and Cartwright, J. (2015). Messinian Evaporites and Fluid Flow. *Mar. Pet. Geology.* 66, 165–176. doi:10.1016/j.marpetgeo.2015.02.003

Bowman, S. A. (2011). Regional Seismic Interpretation of the Hydrocarbon Prospectivity of Offshore Syria. *GeoArabia* 16, 95–124. doi:10.2113/geoarabia160395

Camerlenghi, A., Del Ben, A., Hübscher, C., Forlin, E., Geletti, R., Brancatelli, G., et al. (2020). Seismic Markers of the Messinian Salinity Crisis in the Deep Ionian Basin. *Basin Res.* 32, 716–738. doi:10.1111/bre.12392

Cartwright, J., Huuse, M., and Aplin, A. (2007). Seal Bypass Systems. *Bulletin* 91, 1141–1166. doi:10.1306/04090705181

Chiarabba, C., De Gori, P., and Speranza, F. (2008). The Southern Tyrrhenian Subduction Zone: Deep Geometry, Magmatism and Plio-Pleistocene Evolution. *Earth Planet. Sci. Lett.* 268, 408–423. doi:10.1016/j.epsl.2008.01.036

Cocchi, L., Passaro, S., Tontini, F. C., and Ventura, G. (2017). Volcanism in Slab Tear Faults Is Larger Than in Island-Arcs and Back-Arcs. *Nat. Commun.* 8 (1), 1451. doi:10.1038/s41467-017-01626-w

Conte, A. M., di Bella, L., Ingrassia, M., Perinelli, C., and Martorelli, E. (2020). Alteration and Mineralization Products of the Zannone Giant Pockmark (Zannone Hydrothermal Field, central Tyrrhenian Sea). *Minerals* 10, 581. doi:10.3390/min10070581

Dal Cin, M., del Ben, A., Mocnik, A., Accaino, F., Geletti, R., Wardell, N., et al. (2016). Seismic Imaging of Late Miocene (Messinian) Evaporites from Western Mediterranean Back-Arc Basins. *Pet. Geosci.* 22, 297–308. doi:10.1144/petgeo2015-096

de Mahiques, M. M., Schattner, U., Lazar, M., Sumida, P. Y. G., and Souza, L. A. P. d. (2017). An Extensive Pockmark Field on the Upper Atlantic Margin of Southeast Brazil: Spatial Analysis and its Relationship with Salt Diapirism. *Heliyon* 3, e00257. doi:10.1016/j.heliyon.2017.e00257

De Ritis, R., Pepe, F., Orecchio, B., Casalbore, D., Bosman, A., Chiappini, M., et al. (2019). Magmatism along Lateral Slab Edges: Insights from the Diamante-Enotrio-Ovidio Volcanic-Intrusive Complex (Southern Tyrrhenian Sea). *Tectonics* 38, 2581–2605. doi:10.1029/2019TC005533

Farran, M. (2008). IMAGE2SEGY: Una aplicación informática para la conversión de imágenes de perfiles sísmicos a ficheros en formato SEG Y. *Geo-Temas* 10, 1215–1218.

Franchi, F., Rovere, M., Gamberi, F., Rashed, H., Vaselli, O., and Tassi, F. (2017). Authigenic Minerals from the Paola Ridge (Southern Tyrrhenian Sea): Evidences of Episodic Methane Seepage. *Mar. Pet. Geology.* 86, 228–247. doi:10.1016/j.marpetgeo.2017.05.031

Gamberi, F., and Rovere, M. (2010). Mud Diapirs, Mud Volcanoes and Fluid Flow in the Rear of the Calabrian Arc Orogenic Wedge (southeastern Tyrrhenian Sea). *Basin Res.* 22, 452–464. doi:10.1111/j.1365-2117.2010.00473.x

Geletti, R., Zgur, F., del Ben, A., Buriola, F., Fais, S., Fedi, M., et al. (2014). The Messinian Salinity Crisis: New Seismic Evidence in the West-Sardinian Margin and Eastern Sardo-Provençal basin (West Mediterranean Sea). *Mar. Geology.* 351, 76–90. doi:10.1016/j.margeo.2014.03.019

Hübscher, C., Tahchi, E., Klaucke, I., Maillard, A., and Sahling, H. (2009). Salt Tectonics and Mud Volcanism in the Latakia and Cyprus Basins, Eastern Mediterranean. *Tectonophysics* 470, 173–182. doi:10.1016/j.tecto.2008.08.019

Italiano, F., Romano, D., Caruso, C., Longo, M., Corbo, A., and Lazzaro, G. (2019). Magmatic Signature in Submarine Hydrothermal Fluids Vented Offshore Ventotene and Zannone Islands (Pontine Archipelago, Central Italy). *Geofluids* 2019, 1–15. doi:10.1155/2019/8759609

Iyer, K., Rüpke, L., and Galerne, C. Y. (2013). Modeling Fluid Flow in Sedimentary Basins with Sill Intrusions: Implications for Hydrothermal Venting and Climate Change. *Geochem. Geophys. Geosyst.* 14, 5244–5262. doi:10.1002/2013GC005012

Lawrence, G. W. M., and Cartwright, J. A. (2010). The Stratigraphic and Geographic Distribution of Giant Craters and Remobilised Sediment mounds on the Mid Norway Margin, and Their Relation to Long Term Fluid Flow. *Mar. Pet. Geology.* 27 (4), 733–747. doi:10.1016/j.marpetgeo.2009.10.012

Loreto, M. F., Düşünür-Doğan, D., Üner, S., İşcan-Alp, Y., Ocakoğlu, N., Cocchi, L., et al. (2019). Fault-controlled Deep Hydrothermal Flow in a Back-Arc

Tectonic Setting, SE Tyrrhenian Sea. *Sci. Rep.* 9, 17724. doi:10.1038/s41598-019-53696-z

Lupton, J., De Ronde, C., Sprovieri, M., Baker, E. T., Bruno, P. P., Italiano, F., et al. (2011). Active Hydrothermal Discharge on the Submarine Aeolian Arc. *J. Geophys. Res.* 116, 1–22. doi:10.1029/2010JB007738

Madof, A. S. (2018). Gas Hydrates in Coarse-Grained Reservoirs Interpreted from Velocity Pull up: Mississippi Fan, Gulf of Mexico. *Geology* 46 (6), 559–562. doi:10.1130/G40031.1

Magee, C., Duffy, O. B., Purnell, K., Bell, R. E., Jackson, C. A. L., and Reeve, M. T. (2016). Fault-controlled Fluid Flow Inferred from Hydrothermal Vents Imaged in 3D Seismic Reflection Data, Offshore NW Australia. *Basin Res.* 28, 299–318. doi:10.1111/bre.12111

Malinverno, A. (2012). Evolution of the Tyrrhenian Sea-Calabrian Arc System: The Past and the Present. *Rend. Online Soc. Geol. Ital.* 21, 11–15.

Marani, M., and Gamberi, F. (2004). "Distribution and Nature of Submarine Volcanic Landforms in the Tyrrhenian Sea: the Arc vs the Back-Arc," in *From Seafloor to Deep Mantle: Architecture of the Tyrrhenian Backarc basin. APAT, Memorie Descrittive Della Carta Geologica d'Italia*. Editors M. P. Marani, F. Gamberi, and E. Bonatti, 64, 109–126.

McGinnis, D. F., Greinert, J., Artemov, Y., Beaubien, S. E., and Wüest, A. (2006). Fate of Rising Methane Bubbles in Stratified Waters: How Much Methane Reaches the Atmosphere? *J. Geophys. Res.* 111, 1–15. doi:10.1029/2005JC003183

Milia, A., Turco, E., Pierantoni, P. P., and Schettino, A. (2009). Four-dimensional Tectono-Stratigraphic Evolution of the Southeastern Peri-Tyrrhenian Basins (Margin of Calabria, Italy). *Tectonophysics* 476, 41–56. doi:10.1016/j.tecto.2009.02.030

Minelli, A., Tassetti, A. N., Hutton, B., Pezzuti Cozzolino, G. N., Jarvis, T., and Fabi, G. (2021). Semi-automated Data Processing and Semi-supervised Machine Learning for the Detection and Classification of Water-Column Fish Schools and Gas Seeps with a Multibeam Echosounder. *Sensors* 21 (9), 2999. doi:10.3390/s21092999

Müller, S., Reinhardt, L., Franke, D., Gaedicke, C., and Winsemann, J. (2018). Shallow Gas Accumulations in the German North Sea. *Mar. Pet. Geology.* 91, 139–151. doi:10.1016/j.marpetgeo.2017.12.016

Naudts, L., Greinert, J., Artemov, Y., Beaubien, S. E., Borowski, C., and Batist, M. D. (2008). Anomalous Sea-Floor Backscatter Patterns in Methane Venting Areas, Dnepr paleo-delta, NW Black Sea. *Mar. Geology.* 251, 253–267. doi:10.1016/j.margeo.2008.03.002

Omosanya, K. O., Eruteya, O. E., Siregar, E. S. A., Zieba, K. J., Johansen, S. E., Alves, T. M., et al. (2018). Three-dimensional (3-D) Seismic Imaging of Conduits and Radial Faults Associated with Hydrothermal Vent Complexes (Vøring Basin, Offshore Norway). *Mar. Geology.* 399, 115–134. doi:10.1016/j.margeo.2018.02.007

Passaro, S., Tamburrino, S., Vallefuoco, M., Tassi, F., Vaselli, O., Giannini, L., et al. (2016). Seafloor Doming Driven by Degassing Processes Unveils Sprouting Volcanism in Coastal Areas. *Sci. Rep.* 6. doi:10.1038/srep22448

Pepe, F., Sulli, A., Bertotti, G., and Cella, F. (2010). Architecture and Neogene to Recent Evolution of the Western Calabrian continental Margin: An Upper Plate Perspective to the Ionian Subduction System, central Mediterranean. *Tectonics* 29. doi:10.1029/2009TC002599

Plaza-Faverola, A., Bünz, S., Johnson, J. E., Chand, S., Knies, J., Mienert, J., et al. (2015). Role of Tectonic Stress in Seepage Evolution along the Gas Hydrate-Charged Vestnesa Ridge, Fram Strait. *Geophys. Res. Lett.* 42, 733–742. doi:10.1002/2014GL062474

Procesi, M., Ciotoli, G., Mazzini, A., and Etiope, G. (2019). Sediment-hosted Geothermal Systems: Review and First Global Mapping. *Earth-Science Rev.* 192, 529–544. doi:10.1016/j.earscirev.2019.03.020

Riedel, M., Scherwath, M., Römer, M., Veloso, M., Heesemann, M., and Spence, G. D. (2018). Distributed Natural Gas Venting Offshore along the Cascadia Margin. *Nat. Commun.* 9. doi:10.1038/s41467-018-05736-x

Roelofse, C., Alves, T. M., and Omosanya, K. d. O. (2021). Reutilisation of Hydrothermal Vent Complexes for Focused Fluid Flow on continental Margins (Modgunn Arch, Norwegian Sea). *Basin Res.* 33, 1111–1134. doi:10.1111/bre.12507

Rollet, N., McGiveron, S., Hashimoto, T., Hackney, R., Petkovic, P., Higgins, K., et al. (2012). Seafloor Features and Fluid Migration in the Capel and Faust Basins, Offshore Eastern Australia. *Mar. Pet. Geology.* 35, 269–291. doi:10.1016/j.marpetgeo.2012.03.011

Römer, M., Blumenberg, M., Heeschen, K., Schloemer, S., Müller, H., Müller, S., et al. (2021). Seafloor Methane Seepage Related to Salt Diapirism in the Northwestern Part of the German North Sea. *Front. Earth Sci.* 9. doi:10.3389/feart.2021.556329

Römer, M., Sahling, H., Pape, T., Bohrmann, G., and Spieß, V. (2012). Quantification of Gas Bubble Emissions from Submarine Hydrocarbon Seeps at the Makran continental Margin (Offshore Pakistan). *J. Geophys. Res.* 117, a–n. doi:10.1029/2011JC007424

Rossi, P. L., Bocchi, G., and Lucchini, F. (1980). A Manganese deposit from the South Tyrrhenian Region. *Oceanol. Acta* 3 (1), 107–114.

Rovere, M., Mercorella, A., Frapiccini, E., Funari, V., Spagnoli, F., Pellegrini, C., et al. (2020). Geochemical and Geophysical Monitoring of Hydrocarbon Seepage in the Adriatic Sea. *Sensors (Basel)* 20 (5). doi:10.3390/s20051504

Rovere, M., Gamberi, F., Mercorella, A., Rashed, H., Gallerani, A., Leidi, E., et al. (2014). Venting and Seepage Systems Associated with Mud Volcanoes and Mud Diapirs in the Southern Tyrrhenian Sea. *Mar. Geology.* 347, 153–171. doi:10.1016/j.margeo.2013.11.013

Rovere, M., Rashed, H., Pecchioni, E., Mercorella, A., Ceregato, A., Leidi, E., et al. (2015). Habitat Mapping of Cold Seeps Associated with Authigenic Mineralization (Paola Ridge, Southern Tyrrhenian Sea): Combining Seafloor Backscatter with Biogeochemistry Signals. *Ijg* 134, 23–31. doi:10.3301/IJG.2014.15

Schneider von Deimling, J., Rehder, G., Greinert, J., McGinnnis, D. F., Boetius, A., Linke, P., et al. (2011). Quantification of Seep-Related Methane Gas Emissions at Tommeliten, North Sea. *Continental Shelf Res.* 31, 867–878. doi:10.1016/j.csr.2011.02.012

Serié, C., Huuse, M., and Schødt, N. H. (2012). Gas Hydrate Pingoes: Deep Seafloor Evidence of Focused Fluid Flow on continental Margins. *Geology* 40, 207–210. doi:10.1130/G32690.1

Simoneit, B. R. T., Kawka, O. E., and Brault, M. (1988). Origin of Gases and Condensates in the Guaymas Basin Hydrothermal System (Gulf of California). *Chem. Geology.* 71, 169–182. doi:10.1016/0009-2541(88)90113-1

Svensen, H., Planke, S., Malthe-Sørenssen, A., Jamtveit, B., Myklebust, R., Rasmussen Eidem, T., et al. (2004). Release of Methane from a Volcanic basin as a Mechanism for Initial Eocene Global Warming. *Nature* 429, 542–545. doi:10.1038/nature0257510.1038/nature02566

Svensen, H., Jamtveit, B., Planke, S., and Chevallier, L. (2006). Structure and Evolution of Hydrothermal Vent Complexes in the Karoo Basin, South Africa. *J. Geol. Soc.* 163, 671–682. doi:10.1144/1144-764905-037

Svensen, H., Planke, S., Jamtveit, B. r., and Pedersen, T. (2003). Seep Carbonate Formation Controlled by Hydrothermal Vent Complexes: a Case Study from the Vøring Basin, the Norwegian Sea. *Geo-Marine Lett.* 23, 351–358. doi:10.1007/s00367-003-0141-2

Sydnes, M., Fjeldskaar, W., Grunnaleite, I., Fjeldskaar Løtveit, I., and Mjelde, R. (2019). Transient Thermal Effects in Sedimentary Basins with Normal Faults and Magmatic Sill Intrusions-A Sensitivity Study. *Geosciences* 9, 160. doi:10.3390/geosciences9040160

Würtz, M., and Rovere, M. (2015). *Atlas of the Mediterranean Seamounts and Seamount-like Structures*. IUCN, Malaga, 275 p. ISBN: 978-2-8317-1750-0. doi:10.2305/IUCN.CH.2015.07.en

Waage, M., Portnov, A., Serov, P., Bünz, S., Waghorn, K. A., Vadakkepuliyambatta, S., et al. (2019). Geological Controls on Fluid Flow and Gas Hydrate Pingo Development on the Barents Sea Margin. *Geochem. Geophys. Geosyst.* 20, 630–650. doi:10.1029/2018GC007930

Conflict of Interest: The authors declare that the research was conducted in the absence of any commercial or financial relationships that could be construed as a potential conflict of interest.

Publisher's Note: All claims expressed in this article are solely those of the authors and do not necessarily represent those of their affiliated organizations, or those of the publisher, the editors and the reviewers. Any product that may be evaluated in this article, or claim that may be made by its manufacturer, is not guaranteed or endorsed by the publisher.